Monthly Notices of the ROYAL ASTRONOMICAL SOCIETY

MNRAS **506,** 4578–4592 (2021) https://doi.org/10.1093/mnras/stab2072
Advance Access publication 2021 July 20

# Effects of model incompleteness on the drift-scan calibration of radio telescopes

Bharat K. Gehlot [1]★ Daniel C. Jacobs,[1] Judd D. Bowman,[1] Nivedita Mahesh,[1] Steven G. Murray,[1] Matthew Kolopanis [1] Adam P. Beardsley,[1,2]† Zara Abdurashidova,[3] James E. Aguirre,[4] Paul Alexander,[5] Zaki S. Ali,[3] Yanga Balfour,[6] Gianni Bernardi,[6,7,8] Tashalee S. Billings,[4] Richard F. Bradley,[9] Phil Bull,[10] Jacob Burba,[11] Steve Carey,[5] Chris L. Carilli,[12] Carina Cheng,[3] David R. DeBoer,[3] Matt Dexter,[3] Eloy de Lera Acedo,[5] Joshua S. Dillon,[3]† John Ely,[5] Aaron Ewall-Wice,[13] Nicolas Fagnoni,[5] Randall Fritz,[6] Steven R. Furlanetto,[14] Kingsley Gale-Sides,[5] Brian Glendenning,[12] Deepthi Gorthi,[3] Bradley Greig,[15] Jasper Grobbelaar,[6] Ziyaad Halday,[6] Bryna J. Hazelton,[16,17] Jacqueline N. Hewitt,[13] Jack Hickish,[3] Austin Julius,[6] Nicholas S. Kern,[13] Joshua Kerrigan,[11] Piyanat Kittiwisit,[18] Saul A. Kohn,[4] Adam Lanman,[11] Paul La Plante,[3,4] Telalo Lekalake,[6] David Lewis,[1] Adrian Liu,[19] Yin-Zhe Ma,[20] David MacMahon,[3] Lourence Malan,[6] Cresshim Malgas,[6] Matthys Maree,[6] Zachary E. Martinot,[4] Eunice Matsetela,[6] Andrei Mesinger,[21] Mathakane Molewa,[6] Raul A. Monsalve,[1,19,22] Miguel F. Morales,[16] Tshegofalang Mosiane,[6] Abraham R. Neben,[13] Bojan Nikolic,[5] Aaron R. Parsons,[3] Robert Pascua,[3] Nipanjana Patra,[3] Samantha Pieterse,[6] Jonathan C. Pober,[11] Nima Razavi-Ghods,[5] Jon Ringuette,[16] James Robnett,[12] Kathryn Rosie,[6] Mario G. Santos,[6,23] Peter Sims,[19] Craig Smith,[6] Angelo Syce,[6] Max Tegmark,[13] Nithyanandan Thyagarajan,[12]‡ Peter K. G. Williams[24,25] and Haoxuan Zheng[13]

*Affiliations are listed at the end of the paper*

Accepted 2021 July 14. Received 2021 July 13; in original form 2021 April 24

## ABSTRACT

Precision calibration poses challenges to experiments probing the redshifted 21-cm signal of neutral hydrogen from the Cosmic Dawn and Epoch of Reionization ($z \sim 30$–$6$). In both interferometric and global signal experiments, systematic calibration is the leading source of error. Though many aspects of calibration have been studied, the overlap between the two types of instruments has received less attention. We investigate the sky based calibration of total power measurements with a HERA dish and an EDGES-style antenna to understand the role of autocorrelations in the calibration of an interferometer and the role of sky in calibrating a total power instrument. Using simulations we study various scenarios such as time variable gain, incomplete sky calibration model, and primary beam model. We find that temporal gain drifts, sky model incompleteness, and beam inaccuracies cause biases in the receiver gain amplitude and the receiver temperature estimates. In some cases, these biases mix spectral structure between beam and sky resulting in spectrally variable gain errors. Applying the calibration method to the HERA and EDGES data, we find good agreement with calibration via the more standard methods. Although instrumental gains are consistent with beam and sky errors similar in scale to those simulated, the receiver temperatures show significant deviations from expected values. While we show that it is possible to partially mitigate biases due to model inaccuracies by incorporating a time-dependent gain model in calibration, the resulting errors on calibration products are larger and more correlated. Completely addressing these biases will require more accurate sky and primary beam models.

**Key words:** instrumentation: interferometers – instrumentation: miscellaneous – methods: data analysis – methods: statistical – techniques: interferometric – dark ages, reionization, first stars.

## 1 INTRODUCTION

Observations of the highly redshifted 21-cm signal of neutral hydrogen (H I) from the Cosmic Dawn ($z \sim 30$–$12$) and the Epoch of Reionization ($z \sim 12$–$6$) have the potential to uncover a wealth

★ E-mail: kbharatgehlot@gmail.com
† NSF Astronomy and Astrophysics Postdoctoral Fellow.
‡ NRAO Jansky Fellow.

of information about the properties of the first luminous objects (e.g. first stars and galaxies), intergalactic medium as well as fundamental physics questions. This promising avenue has motivated the development of instruments targeting the low-frequency band. These arrays are both interferometric arrays like e.g. the Giant Meterwave Radio Telescope (GMRT; Paciga et al. 2011), the Low Frequency Array (LOFAR; van Haarlem et al. 2013), the Murchison Widefield Array (MWA; Tingay et al. (MWA; Bowman et al. 2013; Tingay et al. 2013), the Precision Array to Probe Epoch of Reionization (PAPER; now decommissioned; Parsons et al. 2010), the Hydrogen Epoch of Reionization Array (HERA; DeBoer et al. 2017), the Owens Valley Long Wavelength Array (OVRO-LWA; Eastwood et al. 2018; Eastwood et al. 2019), the New Extension in Nançay Upgrading loFAR (NENUFAR; Zarka et al. 2012), and the upcoming Square Kilometer Array (SKA; Mellema et al. 2013; Koopmans et al. 2015), as well as single-receiver radiometers including the Experiment to Detect the Global Epoch of reionization Signature (EDGES; Bowman et al. 2018), the Shaped Antenna measurement of the background RAdio Spectrum-2 (SARAS2; Singh et al. 2017), the Large-aperture Experiment to Detect the Dark Ages (LEDA; Bernardi et al. 2016), and the Probing Radio Intensity at high $z$ from Marion (PRIZM; Philip et al. 2019). All these experiments are working towards measuring the brightness temperature fluctuations of the redshifted 21-cm H I signal and the sky-averaged 21-cm signal (or global 21-cm signal) from the epochs of Cosmic Dawn and Reionization.

The redshifted 21-cm signal (both global signal and fluctuations) is extremely faint. It is contaminated by bright astrophysical foregrounds (Galactic diffuse and free–free emission, supernova remnants, radio galaxies and clusters, etc.) that are several orders of magnitude brighter than the signal of interest, ionosphere of the Earth, and instrumental imperfections, e.g. direction-independent and dependent instrumental response, frequency-dependent instrumental bandpass, polarization leakage, etc. These contaminations make extraction of the 21-cm signal from the observed signal an extremely challenging process.

Calibration of instruments used by 21-cm cosmology experiments is a daunting task and needs to be performed with great accuracy and precision (with an error level $\sim 10^{-5}$) to achieve a dynamic range high enough to detect the faint 21-cm signal. Most interferometric 21-cm cosmology experiments use calibration methods that rely on knowledge of the sky and/or array layout (redundancy between baselines). These methods utilize cross-correlation products to obtain per antenna complex gain (both direction-independent and dependent) that are used to correct the observed cross-correlations (Mitchell et al. 2008; Salvini & Wijnholds 2014; Yatawatta 2015; Li et al. 2018). On the other hand, global 21-cm signal experiments with single-element radiometers use calibration methods that require switching between various loads (see e.g. Pauliny-Toth & Shakeshaft 1962; Rogers & Bowman 2012; Monsalve et al. 2017) and absolute receiver temperature measurements by putting antenna + receiver in anechoic chambers of known temperatures (only possible for miniature antennas, see e.g. An, Nauwelaers & Van de Capelle 1993). However, many experiments have also explored the use of total power sky measurements (or autocorrelations) for various types of calibration, such as bandpass amplitude, signal chain reflection, and mutual coupling calibration (see e.g. Rogers et al. 2004; Ewall-Wice et al. 2016; Monsalve et al. 2017; Singh et al. 2018; Barry et al. 2019; Kern et al. 2019; Li et al. 2019; Mozdzen et al. 2019; Monsalve et al. 2021, HERA memos for various implementations). Various statistical estimators used in 21-cm cosmology interferometric experiments also require correction of bias introduced due to instrumental noise temperature and correct propagation of thermal uncertainties in the analyses (see e.g. Trott et al. 2016; Kolopanis et al. 2019; Mertens et al. 2020). The very high accuracy and precision required in this measurement has led to the exploration of autocorrelation (or total power) based calibration by both types of experiments.

Most methods to calibrate instruments using autocorrelations/total power measurements employ known sky brightness maps and primary beam patterns to obtain calibration products to correct the observed data. Rogers et al. (2004) described one such method that utilizes sky-brightness maps (or their simulations) to calibrate antenna arrays by obtaining gain amplitudes (bandpass) and receiver noise temperature per frequency channel. This method uses measured power or autocorrelations (in case of single element or interferometers, respectively) and known beam averaged sky-brightness temperature as a function of sidereal time and frequency to obtain receiver temperature and bandpass gain amplitude. However, such methods are susceptible to errors and biases due to various factors, such as instrumental instability in time, sky model incompleteness and inaccuracies in the primary beam model used for calibration. Recently, Li et al. (2021) investigated gain, sky temperature, and receiver temperature variations in the MeerKAT receiver system using the correlated ($1/f$) noise analyses of the South Celestial pole tracking observations with MeerKAT.

In this paper, we use simulations of autocorrelations (total power) to investigate various factors that could produce bias in calibration and possible ways to mitigate these biases. We further use delay spectrum analysis to study the effect of model incompleteness on calibration products from autocorrelation-based calibration. This paper is organized as follows: Section 2 defines the autocorrelation-based interferometric calibration method. Section 3 provides a brief description of the instrument models and the autocorrelation simulations we have used for analysis. We discuss various model incompleteness effects in Section 4, and provide a comparison of these effects in delay space in Section 5. In Section 6, we discuss the calibration of HERA and EDGES data using the autocorrelation-based calibration. Finally, we summarize our tests and provide some context discussion in Section 7.

## 2 INSTRUMENTAL CALIBRATION USING AUTOCORRELATIONS/TOTAL POWER MEASUREMENTS

Interferometers correlate every signal from one antenna element with itself (autocorrelations) and signals from other antenna elements (cross-correlations). Typically, in arrays like the JVLA, which are not equipped with Dicke switching radiometers, autocorrelations are usually not employed in calibration. However, responding to the challenge of calibrating on wide fields without signal loss/suppression (Barry et al. 2016; Patil et al. 2016), 21-cm experiments have used autocorrelations to calibrate signal chain reflections (Barry et al. 2019; Li et al. 2019; Kern et al. 2019, 2020a) and to make an independent measure of absolute calibration (see e.g. HERA memo #34; Bowman et al. 2007). The latter is the focus of our investigation here.

For a stable, linear system, autocorrelations (or total power) measured by an antenna element ($R_i$) can be modelled as the sum of the temperature due to sky power ($T_{\rm sky}$) and the receiver noise temperature ($T_{\rm rxr}$) attenuated by the receiver gain ($g_i$):

$$\begin{aligned} R_i(\nu, t) &= g_i(\nu) g_i^*(\nu)(T_{\rm sky}(\nu, t) + T_{\rm rxr}) \\ &= G_i(\nu)(T_{\rm sky}(\nu, t) + T_{\rm rxr})\,. \end{aligned} \quad (1)$$

Note that $g_i$ and $T_{\rm rxr}$ are assumed to be constant in time. For convenience, we use the notation $G_i = |g_i|^2$ hereafter. Though it is standard practice to describe receiver temperature in terms of equivalent sky power, thus making it dependent on gain; in reality, gain and noise are not simply related physical properties. Here, we redefine autocorrelations $R$ in terms of internal noise $n$, resulting in the following equation:

$$R_i(\nu, t) = G_i(\nu)T_{\rm sky}(\nu, t) + n_i(\nu)\,, \tag{2}$$

where $n_i$ is the additional noise bias (referred to as noise figure hereafter) due to the antenna element and can be defined in terms of receiver temperature $T_{\rm rxr} = n/G$. The power due to the sky in temperature units $T_{\rm sky}(\nu, t)$ can be modelled with a sky brightness temperature map $T_{\rm map}$ (see e.g. Haslam et al. 1982; De Oliveira-Costa et al. 2008; Zheng et al. 2017), which is a function of apparent coordinates $(\theta, \phi)$ at time $t$, and frequency $\nu$. Expected sky temperature spectrum $T_{\rm sky}(\nu, t)$ may be calculated as a weighted average of $T_{\rm map}$ with weights determined by the antenna primary beam $A(\theta, \phi, \nu)$:

$$T_{\rm sky}(\nu, t) = \frac{\int_\Omega A(\theta, \phi, \nu)T_{\rm map}(\theta, \phi, \nu, t){\rm d}\Omega}{\int_\Omega A(\theta, \phi, \nu){\rm d}\Omega}\,. \tag{3}$$

Autocorrelations measured by an interferometer may be used to determine the antenna gain amplitude $|g_i|$ and the receiver temperature $T_{\rm rxr}$ if the primary beam of antenna element ($A$) and the brightness temperature of the sky ($T_{\rm map}$) observed by the interferometer is well known. For a given antenna element, equation (2) can be modelled as

$$\boldsymbol{y} = \mathbf{A}\boldsymbol{x} + \boldsymbol{\epsilon}\,, \tag{4}$$

where

$$\begin{aligned}\boldsymbol{y} &= \left[R[0]\ \ldots\ R[t]\right]^T,\\ \boldsymbol{x} &= \left[G\ n\right]^T,\\ \mathbf{A} &= \begin{bmatrix} T_{\rm sky}[0] & \ldots & T_{\rm sky}[t] \\ 1 & \ldots & 1 \end{bmatrix}^T,\end{aligned} \tag{5}$$

and $\boldsymbol{\epsilon}$ is the noise vector. The least-squares fit to equation (4) can be written as

$$\hat{\boldsymbol{x}} = (\mathbf{A}^T\mathbf{C}^{-1}\mathbf{A})^{-1}\mathbf{A}^T\mathbf{C}^{-1}\boldsymbol{y}\,, \tag{6}$$

where $\hat{\boldsymbol{x}}$ is a vector consisting of best-fitting gain ($\hat{G}$) and noise figure ($\hat{n}$). The best-fitting receiver temperature ($\hat{T}_{\rm rxr}$) can then be obtained using the following relation:

$$\hat{T}_{\rm rxr} = \frac{\hat{n}}{\hat{G}}\,. \tag{7}$$

Uncertainties on best-fitting parameters can then be obtained from the covariance of estimated parameters $\mathbf{C}_{\hat{\boldsymbol{x}}}$ given by

$$\begin{aligned}\mathbf{C}_{\hat{\boldsymbol{x}}} &= (\mathbf{A}^T\mathbf{C}^{-1}\mathbf{A})^{-1}\,,\\ {\rm Var}(\hat{G}) &= \hat{\sigma}^2_{00}\,,\\ {\rm Var}(\hat{T}_{\rm rxr}) &= \hat{T}^2_{\rm rxr}\sum_{i,j}(-1)^{i+j}\frac{\hat{\sigma}^2_{ij}}{\hat{x}_i\hat{x}_j}\,,\end{aligned} \tag{8}$$

where $\mathbf{C}$ is covariance of data and $\hat{x}_i$ and $\hat{\sigma}^2_{ij}$ are elements of $\hat{\boldsymbol{x}}$ vector and $\mathbf{C}_{\hat{\boldsymbol{x}}}$ matrix, respectively. Autocorrelations for every frequency channel can be independently calibrated to obtain $\hat{G}$ and $\hat{T}_{\rm rxr}$. The method described above assumes that receiver temperature and antenna gain do not vary over time, the primary beam is accurately known, and the sky model used in the calibration process is accurate. However, several uncertainties in the model, e.g. incomplete knowledge of sky brightness, incorrect beam model, temporal and spectral variations of antenna gains, instrumental effects such as cable reflections and cross-talk between antennas can cause errors and bias in the estimation of $G_i$ and $T_{\rm rxr}$ from autocorrelations. Here, our aim is to quantify the effect of antenna gain variations, incomplete sky model, and incorrect beam model on autocorrelation-based calibration using simulated autocorrelations of HERA dish and dipole-type receivers.

## 3 METHODOLOGY

### 3.1 Instrument models

Here we consider two element types, a drift-scan dish representing HERA and a dipole representing EDGES. In both cases, we make simplifying approximations to the instrument model that allows to control the variations. These approximations are reasonable and generally used in simulations without causing any significant deviations from real instruments.

HERA is a next-generation radio interferometer located in the Karoo desert, South Africa (30.7224°S, 21.4278°E, 1100-m elevation). It is designed to measure the redshifted 21-cm signal of neutral hydrogen from the Cosmic Dawn and Epoch of Reionization ($z$ = 25–6). It is a densely packed drift-scan array of parabolic dishes of 14-m diameter and is currently in the build-out phase. HERA baseline design is highly redundant, with 320 dishes closely packed into a hexagonal 300-m-wide grid and 30 outrigger dishes providing baselines up to 3 km. In the first iteration, HERA used feeds based on PAPER antenna design (dipole feeds) operating in the frequency range of 100–200 MHz (100-MHz operational bandwidth). The final design will have broad-band 'Vivaldi' feeds with the operational frequency bandwidth of 200 MHz (50–250MHz) to cover both Epoch of Reionization and Cosmic Dawn frequencies. Readers are referred to DeBoer et al. (2017) for detailed information about the HERA telescope. The first iteration with the dipole feed was the subject of several performance studies (Thyagarajan et al. 2016; Ewall-Wice et al. 2017; Patra et al. 2018) and used for a deep integration (see e.g. Kern et al. 2019, 2020a,b for HERA Phase-I calibration for 21-cm analyses). The HERA dipole-feed was given detailed studies with simulations by Fagnoni et al. (2021), who produced the beam model that we use here.[1]

As a comparison point, we also include an isolated dipole antenna in our analysis. Though not specifically modelled on a single global experiment, the selected dipole antenna most closely aligns to the EDGES style broad-band dipole. For the dipole receiver, we use a Gaussian type primary beam described as

$$A(\theta) = \frac{1}{\sqrt{\pi}\theta_0}\exp\left[-\left(\frac{\theta}{\theta_0}\right)^2\right], \tag{9}$$

where $\theta$ is the co-latitude (such that $\theta = 0$ at zenith), and $\theta_0$ is calculated from the full width at half-maximum (FWHM) that varies with frequency as

$${\rm FWHM} = 72^\circ\left(\frac{\nu}{140\ {\rm MHz}}\right)^{-1}. \tag{10}$$

The FWHM of the dipole beam is chosen to be 72° at 140 MHz, which is equivalent to the FWHM of the EDGES high band antenna at the same frequency. Additionally, we use an elliptical azimuthal

[1]Beam model files are available at github.com/HERA-Team/HERA-Beams.

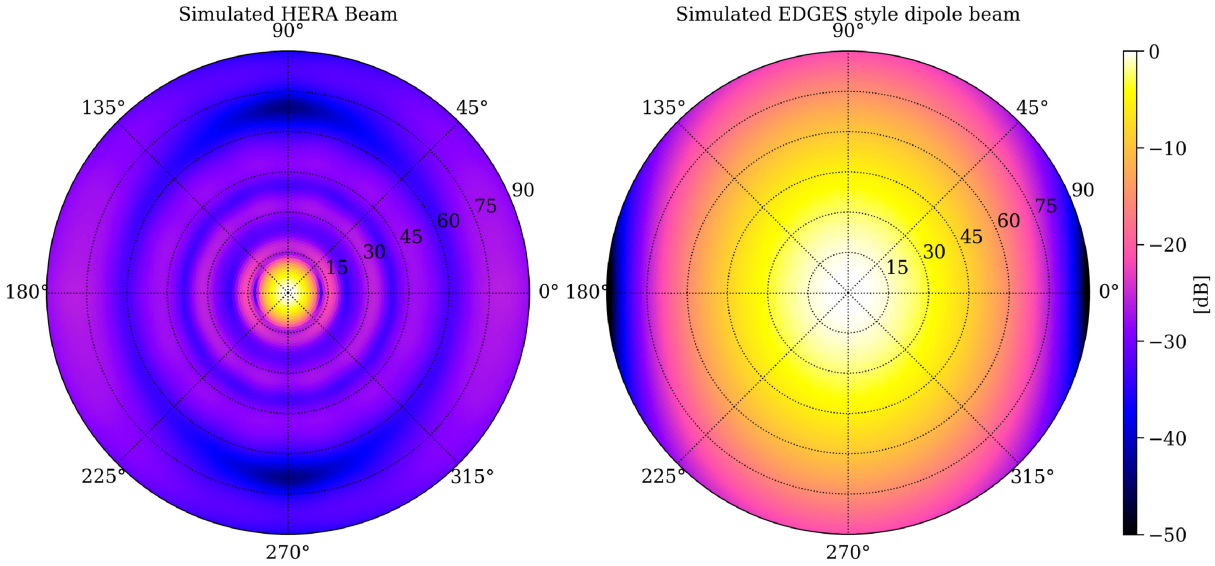


**Figure 1.** Simulated primary beam power patterns for the two types of receiver designs used in the analysis. Left-hand panel: simulated primary beam power pattern (single polarization) of a HERA dish with the dipole feed (PAPER-type). Right-hand panel: simulated primary beam power pattern for a EDGES style dipole (Gaussian-type). Beam patterns are shown in polar projection where the spokes represent azimuth angle, and the dotted circles represent the zenith angle with 15° separation between consecutive circles.

profile for the dipole antenna beam such that the final primary beam pattern becomes

$$A_{\rm dipole}(\theta, \phi) = A(\theta)(\cos^2\phi + \sin^2\phi\cos\theta)^2\,. \tag{11}$$

The final power pattern approximately matches the EDGES antenna primary beam (see e.g. Mahesh et al. 2021). Fig. 1 shows the primary beam power patterns of a single polarization of a HERA dish (with PAPER feed) and the Gaussian dipole. We use these two beam models to simulate autocorrelations for further analyses. Hereafter, the simulated primary beam for the HERA dish will be referred to as the HERA beam, and the simulated EDGES style dipole beam will be referred to as the dipole beam in figures and text.

### 3.2 Simulating mock autocorrelations

We produce mock autocorrelations using the following template:

$$R[\nu, t] = G(T_{\rm sky}[\nu, t] + T_{\rm rxr}) + \epsilon. \tag{12}$$

We choose a receiver temperature $T_{\rm rxr} = 150$ K for both antenna designs and simulate mock autocorrelations for the frequency range $\nu = 110$–$190$ MHz. The above equation also requires averaged sky temperature $T_{\rm sky}[\nu, t]$ as a function of time and frequency. We use equation (3) to calculate spatially averaged sky temperature in the 110–190 MHz frequency range. We use the Global Sky Model (GSM) of diffuse radio emission presented in De Oliveira-Costa et al. (2008, GSM2008 hereafter) to obtain spatially averaged sky temperatures weighted with the HERA and the dipole beams for 0–24 h LST range. Fig. 2 shows averaged sky temperature profiles obtained from GSM2008 for both HERA and dipole beams. The selection of $G$ values to simulate mock autocorrelations is dependent on model incompleteness scenarios we have investigated. For temporal gain variation scenarios, the gain is time-dependent and the gain profile $G[t]$ is set such that it varies around $G_0 = 1$. For other model incompleteness scenarios, the gain is assumed to be constant with value $G = 1$. The mock autocorrelations are sampled at time and frequency intervals of 5 min and 250 kHz, respectively. The uncertainty on autocorrelations ($\sigma_{\rm R}$) is proportional to the antenna temperature $T_{\rm A}$ (sum of the beam-averaged sky temperature $T_{\rm sky}$ and the receiver temperature $T_{\rm rxr}$) and is given by the standard radiometer equation (Wilson, Rohlfs & Hüttemeister 2009):

$$\sigma_{\rm R} = \frac{T_A}{\sqrt{\Delta\nu\Delta t}} = \frac{T_{\rm sky} + T_{\rm rxr}}{\sqrt{\Delta\nu\Delta t}}, \tag{13}$$

where $\Delta\nu$ and $\Delta t$ are integration time and frequency of the instrument and chosen to be $\Delta\nu = 5$ kHz and $\Delta t = 1$ s for both antenna designs. For a given time and frequency, the noise ($\epsilon$) on each autocorrelation value is drawn from Gaussian distributions $\mathcal{N}(0, \sigma_{\rm R}^2)$ with variance given by equation (13).

## 4 EFFECT OF MODEL INCOMPLETENESS

In this section, we explore different effects that may cause errors and bias in $G$ and $T_{\rm rxr}$ estimation. To set a reference, we produce autocorrelations using equation (12), with default values for $G$, $T_{\rm rxr}$ and fit for the parameters as described in Section 2 using the same sky temperature model $T_{\rm sky}$ used to simulate mock autocorrelations. The results are shown in Fig. 3. In an ideal scenario, where the sky temperature and beam model are perfectly known and antenna gain do not change with time and frequency, the calibration parameters $\hat{T}_{\rm rxr}$ and $\hat{G}$ are obtained with small rms error ($\sim 0.2$ per cent on $\hat{G}$ and $\sim 1$ per cent on $\hat{T}_{\rm rxr}$) for both antenna designs i.e. rms($G$) $\sim 0.002$ amn rms($T_{\rm rxr}$) $\sim 1.35$ K for the HERA dish, and rms($G$) $\sim 0.002$ and rms($T_{\rm rxr}$) $\sim 1.64$ K for the dipole antenna. This error is dominated by the uncertainty on mock autocorrelations. We observe that $\hat{T}_{\rm rxr}$ has larger errors at lower frequencies than at higher frequencies due to the spectral dependence of the sky temperature. This spectral dependence affects the error on the additive term in the fitting process leading to larger uncertainty on $\hat{T}_{\rm rxr}$ at the lower end of the frequency band. Moreover, errors on $\hat{G}$ and $T_{\rm rxr}$ for the dipole are larger than for the HERA dish at lower frequencies because $T_{\rm sky}$ for the dipole antenna has less information (independent sky measurements) along the LST direction compared to the HERA dish. In the following sections, we investigate the effect of various types of model incompleteness such

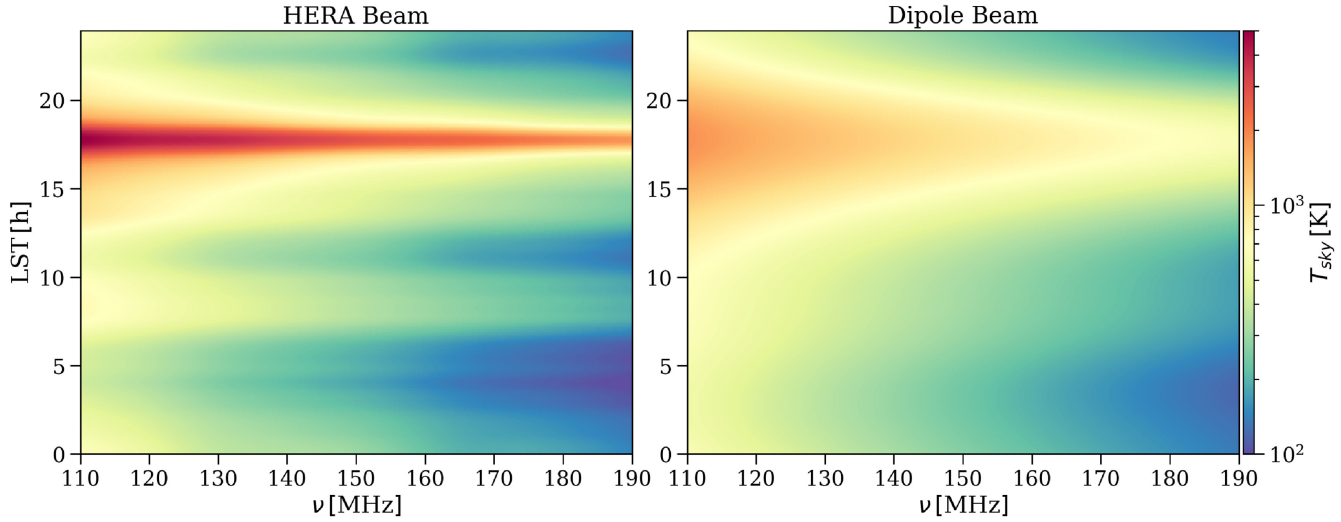


**Figure 2.** Here we show the primary beam averaged sky temperature profiles for the HERA dish (left-hand panel) and dipole type (right-hand panel) receivers as a function of LST and frequency. These profiles were calculated using the GSM2008 sky model of diffuse emission. Large $T_{\rm sky}$ value around LST $= 17.5$ h corresponds to the Galactic Centre transiting through the zenith. Because of the narrower primary beam, the sky temperature profile for the HERA dish shows more structure (and stronger peak for the Galactic Centre transit) along the LST axis compared to the dipole antenna with the wider field of view.

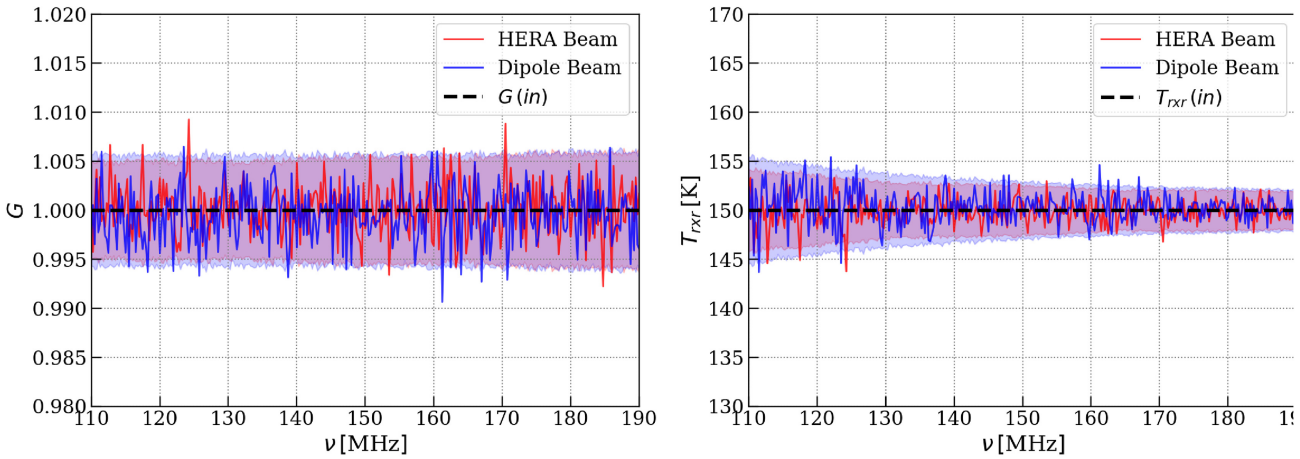


**Figure 3.** Calibration parameters for the reference simulation. Left-hand panel: $\hat{G}$ as a function of frequency for HERA (red curve) and dipole (blue curve) primary beams. Right-hand panel: same as the left-hand panel but for $\hat{T}_{\rm rxr}$. Black dashed lines show input parameter values for autocorrelations simulation. Shaded regions represent the $2\sigma$ error for corresponding parameters. Note that $2\sigma$ errors are placed around the input parameters for a clear representation of error levels. The calibration products fluctuate around input values in simulations with small errors and do not exhibit any visible bias.

as antenna gain variation, sky model incompleteness, and primary beam errors on autocorrelation-based calibration.

### 4.1 Effect of antenna gain variation

The method described in Section 2 assumes an ideal instrument that has stable antenna gains that do not vary with time throughout the observation and has a flat frequency response (bandpass). However, in reality, instruments impart a spectral structure on to the incoming sky signal. They can also have temporally varying antenna gains due to several factors such as ambient temperature variations and unstable electronics. In this section, we study the effect of temporal gain variation on the estimation of $\hat{T}_{\rm rxr}$, and $\hat{G}$ from autocorrelations.

To quantify the effect of temporal variation of antenna gain, we introduce time-dependent gain $G[t]$ in the simulation of mock autocorrelations instead of using a constant $G$ throughout the LST range. For simplification of the analysis, we consider three types of temporal gain variations represented by simple functions: (a) linear variation with LST, (b) sinusoidal variation that correlates with sky brightness, and (c) sinusoidal variation that anticorrelates with sky brightness. Corresponding gain profiles are given by

$$G_{\rm a}[t] = G_0 - 0.1\left(\frac{t}{12} - 1\right),$$
$$G_{\rm b}[t] = G_0 + 0.1\sin\left(\frac{2\pi t}{24}\right),$$
$$G_{\rm c}[t] = G_0 + 0.1\sin\left(2\pi - \frac{2\pi t}{24}\right), \quad (14)$$

where $G_0 = 1$, and $0 \leq t < 24$. The above equations are defined such that $G[t]$ varies around $G_0$ and $0.9 \leq G \leq 1.1$ for all three cases. Fig. 4 shows corresponding gain profiles. Gain drifts caused

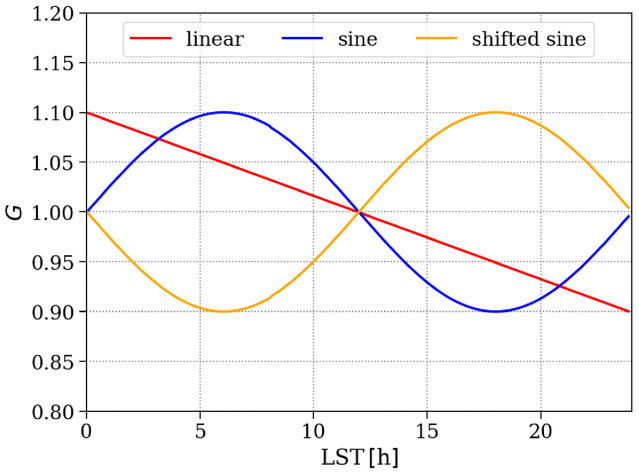


**Figure 4.** Gain profiles $G(t)$ for three types of gain variations with LST used in Section 4.1 to simulate mock autocorrelations. Note that we assume that the instrument has a flat bandpass and the gains only vary in time.

by ambient temperature variations over 24 h are expected to be sinusoidal (profiles b or c). In observations that span shorter LST ranges of the order of a few hours, gain drifts are only a part of the sinusoidal function. These gain drifts can be approximated by type (a) variation. For example, in Kern et al. (2020b), it was reported that average gains for HERA antennas drift by $\sim$ 5–6 per cent over a 6-h range. The drift is approximately linear in time and seems to be anticorrelated with the ambient temperature (as reported by a weather station nearby). Additionally, gain drifts due to diurnal temperature variations are expected to follow similar behaviour as the latter two cases.

We use the above-described gain profiles to generate mock autocorrelations and calibrate those using the GSM2008 sky model to obtain a single $\hat{G}$ and $\hat{T}_{\rm rxr}$ value (per frequency channel) for 24 h of simulated autocorrelations such that complete behaviour of gain drifts is captured. The parameters obtained for different gain variation scenarios are shown in Fig. 5. Because mock autocorrelations have a time-dependent gain, the obtained parameters are biased. The bias level is different for different types of gain drift and is also dependent on antenna design with larger bias for antennas with wider field of view.

We note that the bias in $\hat{G}$ for the HERA beam (top left-hand panel in Fig. 5) shows a weak spectral ripple (peak to peak variation of $\sim$1 per cent) for all three gain variation scenarios. This is caused by the spectral variation in the HERA primary beam coupling into the model. The autocorrelations for a given frequency channel are brightest when the Galactic Centre is in the field of view. During these LSTs, the sky model displays a spectral ripple on a 30-MHz period. Under the proposed theory, gain varies with time causing times with the ripple to receive slightly more weight. Tests excluding the Galactic Centre significantly reduce the ripple. Comparing the gain variation profiles in Fig. 4, we see that $\hat{G}$ that gain amplitude correlates or anticorrelates with Galactic Centre LSTs. The $\hat{T}_{\rm rxr}$ values show an opposite trend because of the inverse dependence on gain. This effect is exclusive to the HERA beam that uses a fully frequency-dependent EM simulation. $\hat{G}$ for the dipole beam, which uses a Gaussian, is approximately constant. In addition to this, the bias in $\hat{T}_{\rm rxr}$ for both antenna designs shows an increase in estimated values as frequency decreases. Spectral dependence of the sky temperature is likely the cause of this increase, leading to larger residuals (hence larger bias) at lower frequencies. This suggests that temporal gain drifts of $\sim$ 10 per cent over 24 h can introduce significant bias in both $\hat{G}$ and $\hat{T}_{\rm rxr}$, which is also dependent on the primary beam passband. Antenna designs with a narrower field of view show relatively lower bias in $\hat{T}_{\rm rxr}$ (approximately similar bias levels in $\hat{G}$).

For the HERA antenna, the rms uncertainty on $\hat{G}$ with respect to its rms amplitude is similar for linear and sinusoidal type gain variations and relatively lower for sinusoidal variations that anticorrelate with the Galactic Centre LST with corresponding levels rms($G_{\rm a}$) $\sim$ 1.05, rms($G_{\rm b}$) $\sim$ 1.03, and rms($G_{\rm c}$) $\sim$ 0.73 per cent, respectively. The rms uncertainty in $\hat{T}_{\rm rxr}$ however are similar for linear and sinusoidal type variations with corresponding rms levels of rms($T_{\rm a}$) $\sim$ 2.8 and rms($T_{\rm b}$) $\sim$ 2.4 per cent but is relatively larger for variations that anticorrelate with the Galactic Centre with rms level of rms($T_{\rm c}$) $\sim$ 4.05 per cent. The uncertainties on the calibration parameters for the dipole antenna are slightly smaller than for the HERA antenna but show a similar behaviour. The rms uncertainty (with respect to the rms amplitude) on $\hat{G}$ and $\hat{T}_{\rm rxr}$ is rms($G$) $\sim$ 1.04, 0.92, 0.61 and rms($T$) $\sim$ 2.8, 2.2, 4.7 per cent for (a), (b), and (c) types of gain variations, respectively. Note that the uncertainties for both antenna designs are smaller than the bias in all three cases of gain variation.

### 4.2 Time-dependent gain model

In Section 4.1, we observed that in realistic cases where the receiver gain changes over time, fitting a constant gain term introduces significant bias in $\hat{G}$ and $\hat{T}_{\rm rxr}$. A viable method to mitigate this bias in calibration products is to incorporate gain time dependence in calibration and fitting for a polynomial gain term to account for temporal variation. In this section, we explore the addition of gain time dependence in the calibration method itself and fit for $\hat{G}(t)$ and $\hat{T}_{\rm rxr}(t)$. As a simple test case, we use a first-order polynomial to represent gain in calibration, i.e. a linear function of LST per channel. The modified fitting template becomes

$$R[t] = (G_0 + G_1 \times t) \times T_{\rm sky}[t] + (n_0 + n_1 \times t), \tag{15}$$

where $G_0$ , $G_1$, $n_0$, and $n_1$ are fitting parameters. Calibration products $\hat{G}$ and $\hat{T}_{\rm rxr}$ can be obtained from these parameters as

$$\begin{aligned} \hat{G} &= \hat{G}_0 + \hat{G}_1 \times t\,, \\ \hat{T}_{\rm rxr} &= \frac{\hat{G}_0 + \hat{G}_1 \times t}{\hat{n}_0 + \hat{n}_1 \times t}\,. \end{aligned} \tag{16}$$

We use mock autocorrelations produced for case (a) in Section 4.1 for this analysis and fit for $\hat{G}(t)$ and $\hat{T}_{\rm rxr}(t)$. The above-described fitting template should be able to capture the linear gain variation in mock autocorrelations perfectly. Fig. 6 shows the corresponding calibration products averaged over time (top row) and frequency (bottom row). Note that the error bars on the averaged estimated parameters are the rms of the uncertainties from the fit along the frequency and time axes, respectively. We observe that bias in both $\hat{G}$ and $\hat{T}_{\rm rxr}$ is mitigated by incorporating a time dependence of gain in calibration. However, the error on the fit for both antenna designs is larger compared to the reference case. As in the reference case, the calibration parameters for the dipole antenna show relatively larger uncertainty compared to the HERA antenna. The rms uncertainty on $\hat{G}$ and $\hat{T}_{\rm rxr}$ are rms($G$) $\sim$ 0.7 and rms($T$) $\sim$ 1.52 per cent for the HERA antenna and rms($G$) $\sim$ 0.9 and rms($T$) $\sim$ 2.2 per cent for the dipole antenna. The uncertainty on $\hat{T}_{\rm rxr}$ for both antenna designs exhibits a frequency dependence, decreasing by a factor of about 2 between the lowest and the highest frequency; however it does not show any prominent spectral dependence in the case of $\hat{G}$. This behaviour is similar to that observed in the reference simulation, i.e.

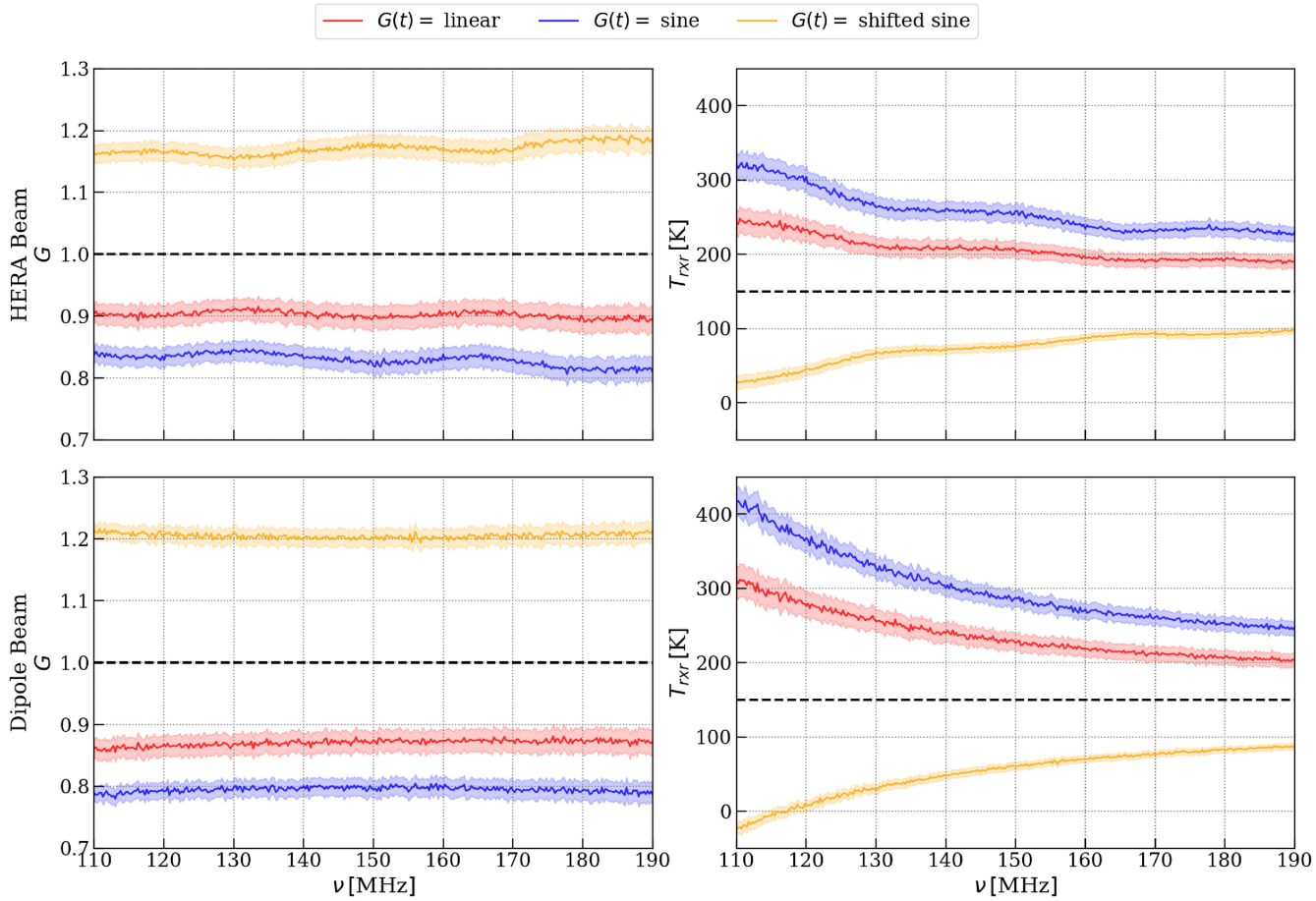


**Figure 5.** Calibration products for simulations with time-dependent gain $G(t)$ (three types of gain variations) for the two antenna designs (top and bottom rows). Left-hand column: $\hat{G}$ obtained from the calibration as a function of frequency. Right-hand panel: same as the left-hand panel but for $\hat{T}_{\rm rxr}$. Dashed lines in the left-hand column correspond to the time-averaged profile of input gain ($\langle G \rangle_t$). Calibration products are biased for all three types of gain variations and corresponding uncertainties are smaller than the bias for both $\hat{G}$ and $\hat{T}_{\rm rxr}$.

the spectral dependence of the sky affects the error on the additive term in the fit. We also notice that the fit is dominated by the LST range with the Galactic Centre above the horizon (12–24 h) for which we see relatively small rms error compared to other LSTs.

In this analysis, we used a simple toy model to describe and mitigate the time dependence of antenna gain and the bias introduced in $\hat{G}$ and $\hat{T}_{\rm rxr}$ due to the same. However, in realistic cases, gain variation might be more sophisticated (e.g. sinusoidal), especially for observations covering the full LST and may not be approximated by a simple linear function. In such cases, the use of higher order polynomials or other basis functions in calibration may be required (see e.g. Wang et al. 2021) where Legendre polynomials are utilized similarly to calibrate the MeerKAT autocorrelation data). Additionally, prior understanding about instrumental gain drift and the LST dependence of ambient temperature may be used to account for temporal gain dependence in calibration.

### 4.3 Effect of sky incompleteness

Autocorrelations-based calibration requires prior knowledge of sky brightness to obtain calibration products $\hat{G}$ and $\hat{T}_{\rm rxr}$. Sky models used in most interferometric calibration methods (either sky-based or using autocorrelations) are mainly based on radio sky surveys, e.g. VLSS (Cohen et al. 2007), GLEAM (Hurley-Walker et al. 2016), LOTSS (Shimwell et al. 2017, 2019), and SSS (Heald et al. 2015) carried out using various radio interferometers, as well as models and maps of diffuse Galactic emission, e.g. GSMs of diffuse emission (GSM2008; Zheng et al. 2017) and LWA diffuse sky maps (Dowell et al. 2017; Eastwood et al. 2018). However, these surveys/maps will all, whether due to calibration, reconstruction, processing, or simply thermal noise, have inherent inaccuracy at some level. In the case of wide-field 21-cm arrays, sensitive in most cases to the entire visible sky, the most relevant limitation is an incomplete sky coverage or missing model flux at relevant size scale. When used for calibration, an incomplete sky model tends to introduce various errors in calibration products at different levels depending on the incompleteness. The impact of model incompleteness on interferometric calibration manifests as baseline-dependent spectral structure that, unchecked, couples to all baselines during the calibration process (Barry et al. 2016; Patil et al. 2016; Ewall-Wice et al. 2017). In the autocorrelations, spatial structure emerges as time dependence, so it is worth investigating whether the spatial-spectral modulation leads to similar issues.

For this analysis, we assume that gains are stable in time and do not have a frequency structure (spectral structure due to the beam remains). Since sky model inaccuracy is a candidate for calibration bias, as a proxy for error, we use the older GSM model (GSM2008; De Oliveira-Costa et al. 2008) as the true sky and the newer GSM

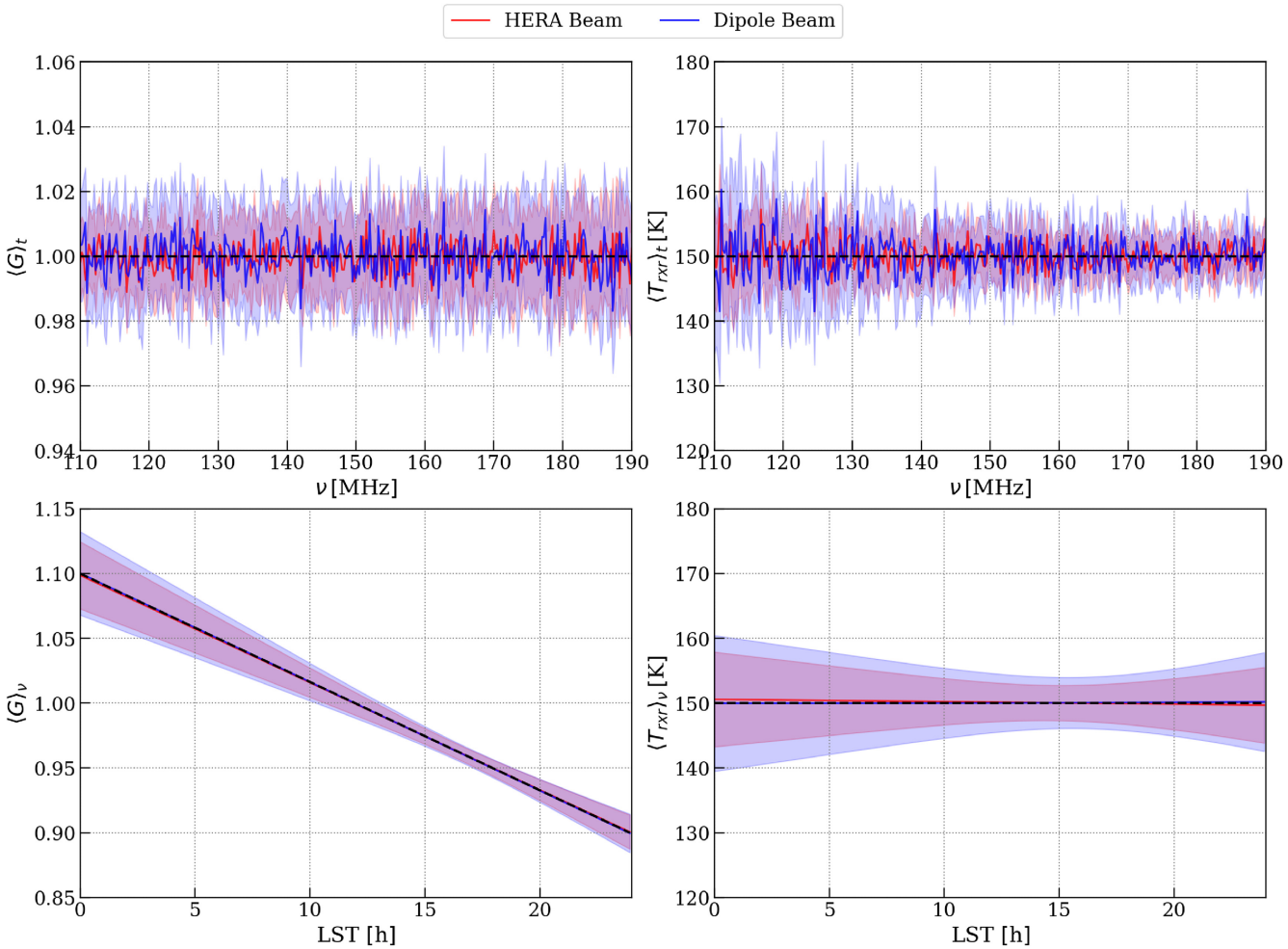


**Figure 6.** Calibration products for the modified calibration that uses first-order polynomials to fit for linear time-dependent gain $G(t)$ (see Section 4.2). The top and bottom rows show calibration parameter $\hat{G}$ (left-hand column) and $\hat{T}_{\rm rxr}$ (right-hand column) averaged over time and frequency, respectively. Dashed lines show the input parameters averaged over corresponding axes. Shaded regions represent rms of error on the fit along the corresponding time and frequency axes used for averaging. Using a first-order polynomial in calibration mitigates the bias in calibration products due to temporal gain variations. However, corresponding uncertainty levels are increased relative to the reference case.

model (Zheng et al. 2017, GSM2016 hereafter) as the input sky model for calibration. The most notable difference between the two GSM models is that in the 2017 update, point sources have been removed. Point sources contribute a small fraction of the total power, emerging primarily as temporal variations on the scale of the beam crossing time; around half an hour for HERA, 3 h for the dipole. However, the average spectrum of GSM2016 exhibits an artificial feature at 150 MHz (abrupt change in total amplitude) that may introduce unusual spectral behaviour in calibration products. To avoid such complications, we extrapolate the GSM2016 map at 200 MHz to the desired frequency range using a spectral index $\beta = -2.4$. The spatial and spectral differences between GSM2008 and GSM2016 models provide a reasonable mismatch between the true sky and the sky model used for calibration. Fig. 7 shows the rms of the fractional difference (in per cent) between the primary beam averaged sky temperature for the two models along time and frequency axis, respectively. Beam-averaged sky temperatures for the two models differ from each other by approximately 5–12 per cent depending on LST and frequency. However, in the case of the HERA antenna, the spatial differences become more prominent due to its narrower field of view and appear as additional temporal structure compared to the dipole antenna with the wider field view that averages out finer spatial structures. Additionally, these variations are most prominent at LSTs when the Galactic Centre is above the horizon.

Fig. 8 shows the calibration products when using an incomplete sky model for calibration. We observe that the incomplete sky model, when used for calibration, introduces bias in both $\hat{G}$ and $\hat{T}_{\rm rxr}$. For a given frequency channel, the amplitude of bias depends upon the level of sky-incompleteness, i.e. difference between the true sky and the sky model used for calibration. We also calculate the expected $T_{\rm rxr}$ values (dotted curves in the right-hand panel of Fig. 8) by dividing the already known noise figure (used to simulate corresponding autocorrelations) by $\hat{G}$ obtained from calibration. We observe that these $T_{\rm rxr}$ values are close to $\hat{T}_{\rm rxr}$ values obtained from the calibration rather than the input $T_{\rm rxr}$, suggesting that the sky incompleteness used in the analysis affects $\hat{G}$ more than the noise figure ($\hat{n}$) obtained from the calibration. In other words, the bias in $\hat{T}_{\rm rxr}$ is mainly due to the bias in $\hat{G}$ rather than $\hat{n}$. The rms error on $\hat{G}$ and $\hat{T}_{\rm rxr}$ have values rms($G$) $\sim 0.3$ and rms($T$) $\sim 1$ per cent for both antenna designs, which is similar to error levels in the reference simulation. The sky model incompleteness at a certain level affects $\hat{G}$ for both narrow and wide-field antenna designs the same way. However, the bias in $\hat{T}_{\rm rxr}$

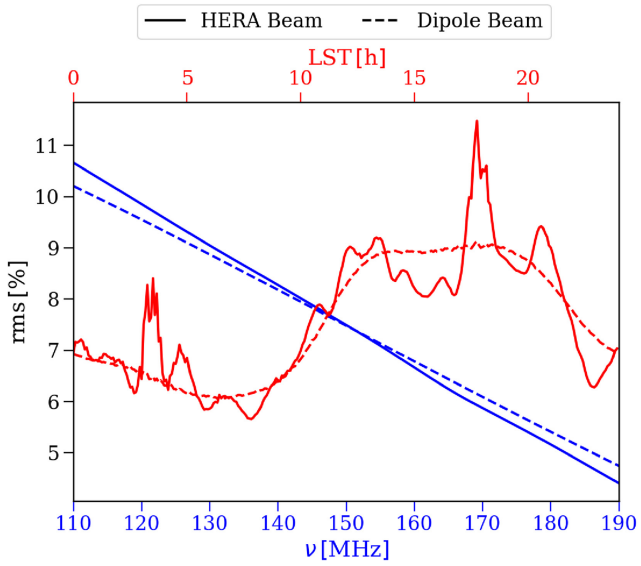


**Figure 7.** Comparison between beam averaged sky temperatures $T_{\rm sky}$ obtained using GSM2008 and GSM2016 models for the two antenna designs. THe GSM2016 model shown here is the GSM2016 skymap at 200 MHz extrapolated to the required frequency range using a spectral index $\beta = -2.4$ unlike GSM2008 model produced for every frequency channel. Blue curves correspond to the rms of the fractional difference $(100 \times (T_{\rm sky}(\text{GSM2008}) - T_{\rm sky}(\text{GSM2016}))/T_{\rm sky}(\text{GSM2008})$ taken over time axis for the two antenna designs. Red curves show the rms of the fractional difference taken over the frequency axis.

is relatively higher for the dipole beam at the lower frequency end compared to the HERA beam. Comparing Figs 7 and 8, we notice that the calibration of autocorrelations with an incomplete sky model introduces a spectrally varying bias in $\hat{G}$ that is dependent on the sky model incompleteness level at corresponding frequencies. Therefore, it becomes evident that sky model incompleteness can play a crucial role in autocorrelation-based interferometric calibration.

### 4.4 Effect of inaccurate primary beam

The sky temperature model used for calibration, as described in Section 2, is the primary beam weighted average of the brightness temperature in every direction of the visible sky. The primary beam model used to calculate the average sky temperature needs to be accurate to obtain unbiased and accurate calibration products $\hat{G}$ and $\hat{T}_{\rm rxr}$. However, measurement of the primary beam for a given antenna is a daunting task by itself. Methods to estimate primary beams include electromagnetic simulations of radio antennas using software packages e.g. CST or FEKO (Fagnoni et al. 2021; Mahesh et al. 2021), holographic beam mapping techniques (Berger et al. 2016; Iheanetu et al. 2019; Asad et al. 2021), beam mapping using bright radio sources transiting through the sky (Baars et al. 1977; Nunhokee et al. 2020) as well as artificial sources e.g. satellites (Neben et al. 2016; Line et al. 2018), and more recently using artificial radio sources mounted on Unmanned Aerial Vehicles (e.g. drones; Chang et al. 2015; Jacobs et al. 2017). Primary beam models obtained from these methods unavoidably contain small errors and thus differ (spatially and spectrally) from true antenna beams. Therefore, using these models may impact the calibration and possibly introduce bias in calibration. In this section, we study the effect of inaccurate primary beam models on autocorrelation-based calibration.

For this analysis, we use an analytical Airy beam instead of the HERA beam used in previous sections to simplify the application of errors to the beam model. We define the analytical Airy beam model as

$$A(\theta) = \left[\frac{2J_1(\pi D \sin\theta/\lambda)}{\pi D \sin\theta/\lambda}\right]^2 , \tag{17}$$

where $D = 14$ m is the diameter of the HERA dish, and $J_1(x)$ is the Bessel function of first kind and order one. To represent primary beam inaccuracies for the Airy and dipole beams, we assume that primary beams are known with $< 10$ per cent errors within the main-lobe and have inaccuracies of $\approx 10$ per cent for side-lobes, similar to the realistic errors reported in Neben et al. (2015) for MWA tile beam patterns. We use a similar approach as Ewall-Wice et al. (2017) to describe the beam errors. We describe the measured beam model (with errors) as

$$A_E(\theta, \phi) = A_0(\theta, \phi)\,[1 + f(\theta)]^2 , \tag{18}$$

where $A_0(\theta, \phi)$ is the true beam and $f(\theta)$ is the fractional error applied to the true beam. $f(\theta)$ is written as

$$f(\theta) = \begin{cases} 1 - (1 - e_z)\exp(-\sin^2\theta/2\sigma_{\rm e}^2) & |\sin\theta| < s_1 \\ 1 - (1 - e_z)\exp(-s_1^2/2\sigma_{\rm e}^2) & |\sin\theta| \geq s_1 \end{cases}, \tag{19}$$

where $e_z = 0.06$ and the parameter $s_1$ is given by

$$\begin{aligned} s_1^{\rm Airy} &= \frac{7.0156\lambda}{\pi D} , \\ s_1^{\rm dipole} &= \sin(0.5 \times \text{FWHM}) , \end{aligned} \tag{20}$$

which is equivalent to the sine of the angular distance of the second null from the pointing centre in case of the Airy beam and sine of angular distance between the pointing centre and the half-power point of the main-lobe (half of the FWHM) in case of the dipole beam. We define $\sigma_{\rm e} = 1.5 s_1$ to introduce frequency dependence in the fractional error. The parameters $e_z$, $s_1$, and $\sigma_{\rm e}$ are set such that uncertainties approximately match the levels mentioned earlier. Fractional error profiles $(A_0(\theta, \nu)f^2(\theta, \nu))$ as a function of zenith angle and frequency for the two beams are shown in Fig. 9.

We simulate the mock autocorrelations using the ideal beam models without any error term $(A_0(\theta, \phi))$ whereas the sky models used as the input for calibration incorporate the measured beam model described by equation (18). Calibration products as a function of frequency for this analysis are shown in Fig. 10. We observe that the effect of primary beam inaccuracies is somewhat similar to that of sky model incompleteness as discussed in Section 4.3. An inaccurate beam model used for calibration seems to affect the dipole beam worse than the Airy beam. The bias in $\hat{G}$ for the Airy beam is small enough that the estimated gain, for the most part, agrees with the input value, whereas $\hat{T}_{\rm rxr}$ deviates from the input especially towards lower frequencies. On the other hands, calibration parameters for the dipole beam show bias with a steeper spectral dependence. We expect this behaviour to be solely dependent on overall inaccuracy introduced in $T_{\rm sky}$ due to the fractional error on the primary beam used for calibration. The expected $T_{\rm rxr}$ values (dotted curves in Fig. 10) for both antenna designs are similar to the input $T_{\rm rxr}$ suggesting that the bias in the noise figure $\hat{n}$ obtained from calibration dominates the bias in $\hat{T}_{\rm rxr}$. The uncertainties on $\hat{G}$ and $\hat{T}_{\rm rxr}$ for the Airy beam are similar to the reference simulation, i.e. $\text{rms}(G) \sim 0.3$ and $\text{rms}(T) \sim 1$ per cent, whereas the calibration parameters for the dipole beam show larger uncertainty with rms values of $\text{rms}(G) \sim 0.4$ and $\text{rms}(T) \sim 1.5$ per cent. This analysis demonstrates that inaccurate beam models used in the calibration of autocorrelations introduce spectral structures in both gain and

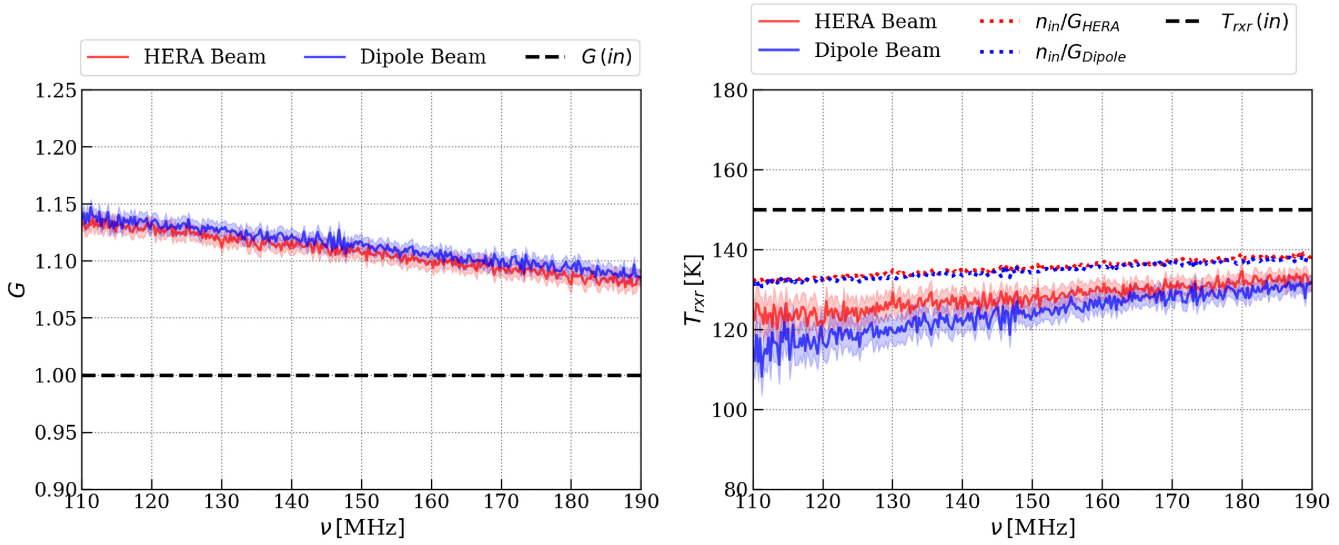


**Figure 8.** Fitting parameters for calibration using an incomplete sky model with incompleteness levels shown in Fig. 7. Left-hand panel: $\hat{G}$ obtained from calibration for HERA and dipole primary beams. Right-hand panel: same as the left-hand panel but for $T_{\rm rxr}$. Dotted curves show $n_{\rm in}/\hat{G}$, i.e. expected $T_{\rm rxr}$ for the two antenna designs obtained from calibrated gains $\hat{G}$ shown in the left-hand panel and already known noise figure ($n_{\rm in}$). Sky model incompleteness introduces spectrally varying bias in calibration products at similar levels for both antenna designs.

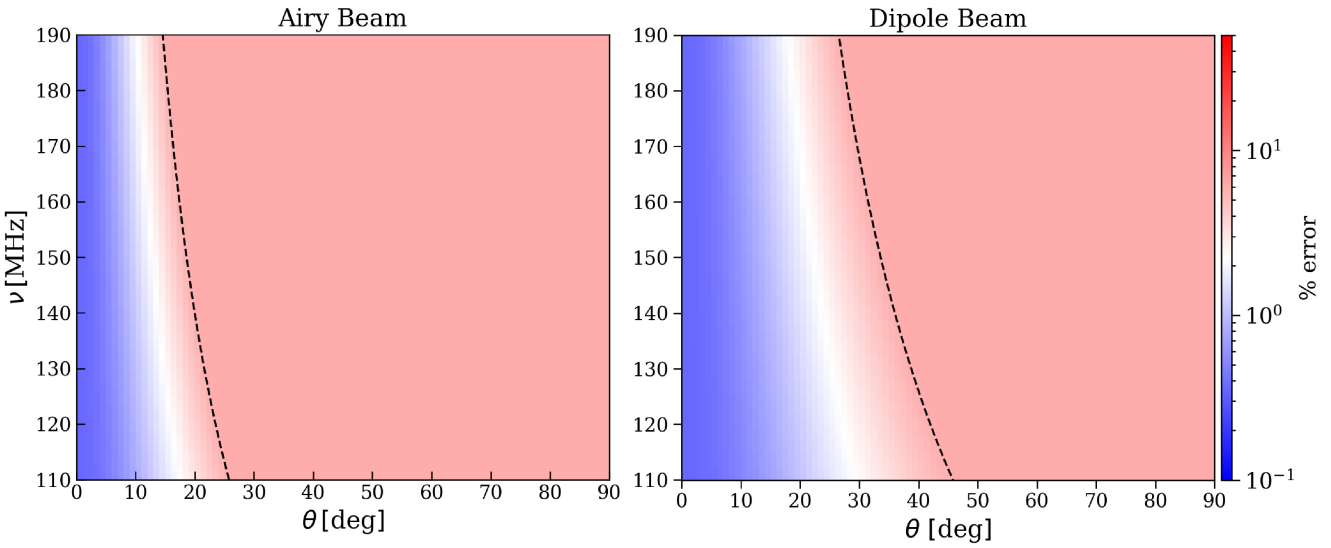


**Figure 9.** Fractional error profiles for the Airy beam (left-hand panel) and the dipole beam (right-hand panel). The dotted line corresponds to $\sin^{-1}(s_1)$, which represents the transition angle. Below this angle, the fractional error is $< 10$ per cent, while above this angle, the error is equal to 10 per cent.

receiver temperature estimates with levels dependent upon the magnitude of beam inaccuracy and field of view of antenna elements. Additionally, primary beam inaccuracies seem to affect $\hat{n}$ more severely compared to $\hat{G}$, making the former a leading cause of bias in $\hat{T}_{\rm rxr}$.

## 5 DELAY SPECTRUM ANALYSIS

As we observed in previous sections, incompleteness effects such as temporal variation of instrumental gain, sky model incompleteness and primary beam inaccuracies introduce addition spectral structure in the calibration products $\hat{G}$ and $\hat{T}_{\rm rxr}$. When applied to the data, these calibration products may leak smooth foregrounds to otherwise clean modes in Fourier space. We use the delay transform technique to investigate this further.

Delay transform is a widely used diagnostic tool and a statistic in 21-cm experiments (Parsons et al. 2012; Liu, Parsons & Trott 2014). The delay spectrum is defined as the Fourier transform of a visibility spectrum observed by a given interferometric baseline along the frequency direction. The delay parameter $\tau$ is the Fourier dual to the frequency and corresponds to the time delay between the signal arriving (from a particular direction) at the two antennas of a given baseline. Although the delay spectrum is defined for a visibility, the methodology can also be applied to autocorrelations and other parameters such as gain and receiver temperature. A delay spectrum of any parameter with a frequency spectrum $F(\nu)$ is defined

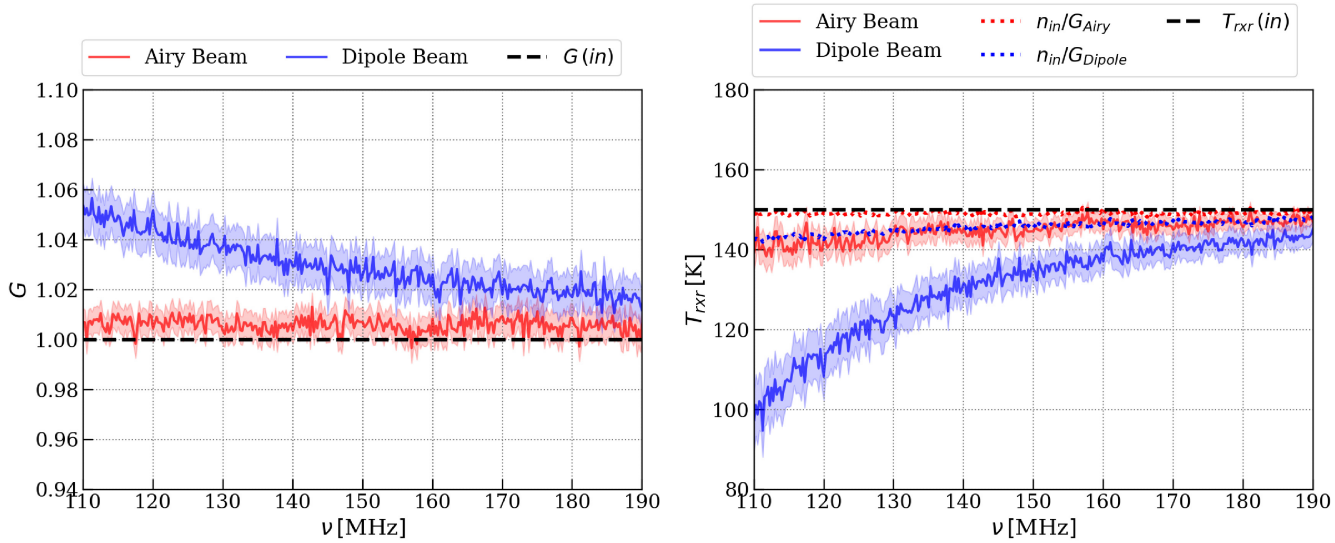


**Figure 10.** Calibration products for the calibration with an inaccurate beam model as described in Section 4.4. Left-hand panel: $\hat{G}$ as a function of frequency for the Airy (red) and dipole (blue) beam. Right-hand panel: same as the left-hand panel but for $\hat{T}_{\rm rxr}$. Dotted curves show $n_{\rm in}/\hat{G}$, i.e. expected $T_{\rm rxr}$ for the two antenna designs obtained from calibrated gains $\hat{G}$ shown in the left-hand panel and already known noise figure ($n_{\rm in}$). The dipole beam shows higher bias than the Airy beam.

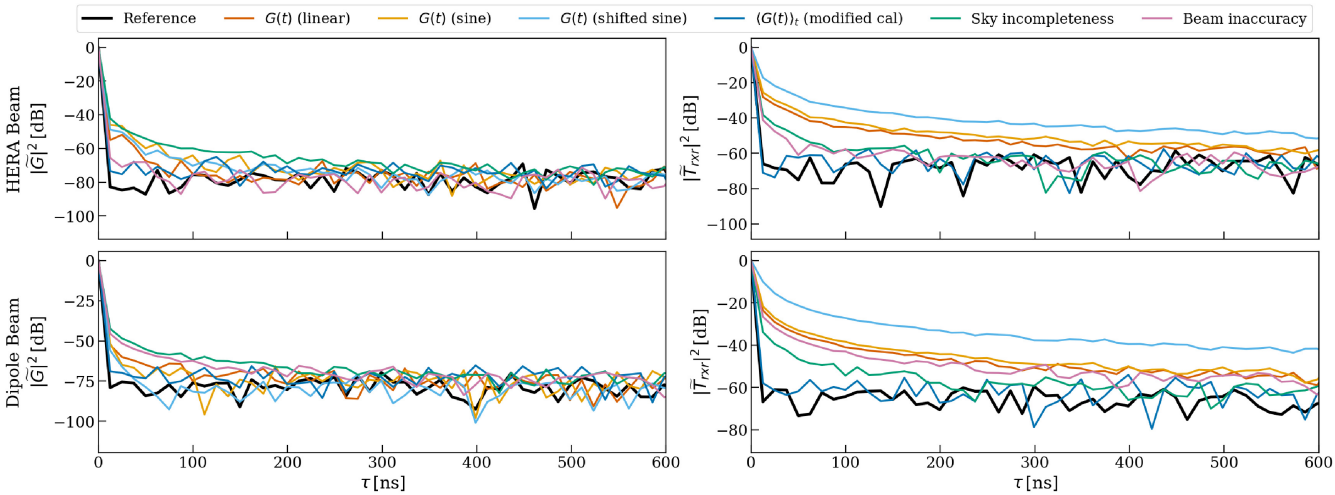


**Figure 11.** A delay space comparison of calibration products $\hat{G}$ (left-hand column) and $\hat{T}_{\rm rxr}$ (right-hand column) for different model incompleteness scenarios. The top and bottom rows correspond to HERA and dipole primary beams, respectively.

as

$$\tilde{F}(\tau) = \int \mathrm{e}^{2\pi i \nu \tau} F(\nu) \mathrm{d}\nu \,. \tag{21}$$

We compare the cases where model incompleteness incurs frequency-dependent bias in calibration products $\hat{G}$ and/or $\hat{T}_{\rm rxr}$ viz. temporal variation of antenna gain, sky incompleteness and primary beam inaccuracies, with the reference simulation. Additionally, we compare output products from the calibration method utilizing the time-dependent gain model (Section 4.2) with the above-mentioned cases. Fig. 11 shows the delay space comparison of calibration products $\hat{G}$ and $\hat{T}_{\rm rxr}$ for different model incompleteness scenarios discussed in Section 4. Note that the spectra are normalized with corresponding $\tau = 0$ power. It essentially removes the mean bias in calibration products, and only the spectral structure remains. For both antenna designs (HERA/Airy beam and dipole beam), delay spectra of estimated gains ($\hat{G}$) for temporal gain variations show additional power on small delay modes ($\tau < 100$ ns) compared to the reference simulation. However, the additional power is not as prominent compared to the sky-incompleteness case. On the other hand, delay spectra of $\hat{T}_{\rm rxr}$ show additional power on a wider range of delay modes especially in temporal gain variations. As discussed in Section 4.2, we modified the calibration to fit for a first-order polynomial as a function of time to describe gain ($G$) and the noise figure ($n$). Here also, we observe that using a time-dependent model for gain and noise figure in calibration mitigates the additional power caused by temporal gain drifts in delay spectrum of $\langle \hat{T}_{\rm rxr} \rangle_t$ on small delay modes and the resulting delay spectra for both $\langle \hat{G} \rangle_t$ and $\langle \hat{T}_{\rm rxr} \rangle_t$ approximately match the reference simulation.

Sky model incompleteness also causes the power to leak to higher delays ($\tau < 200$ ns) in both $\hat{G}$ and $\hat{T}_{\rm rxr}$ delay spectra. Leakage of power to higher delays in $\hat{G}$ due to sky incompleteness is strongest

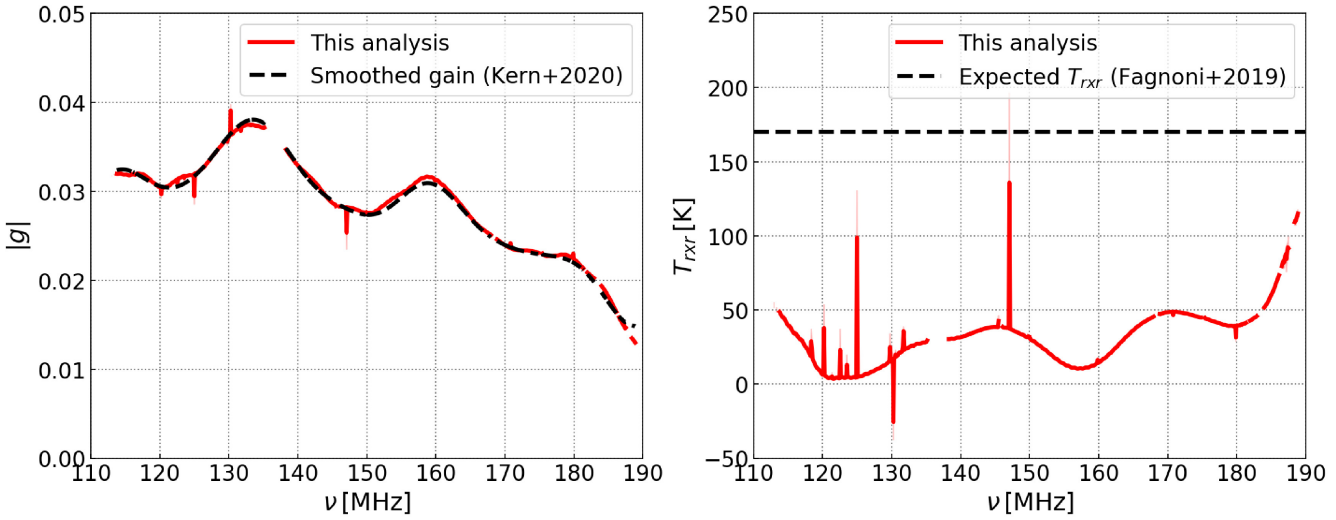


**Figure 12.** Calibration products obtained after calibrating the HERA autocorrelations with the method described in Section 2. Red curves show $|g| = \sqrt{\hat{G}}$ and $\hat{T}_{\rm rxr}$ averaged over eight antennas. The corresponding uncertainties (rms of the error on the fit over eight antennas) are very small with levels rms$|g| < 0.1$ per cent and rms$T \sim 1$ per cent and are not visible. The dashed curves in left- and right-hand panels correspond to the smoothed gain amplitude $|g|$ averaged over eight antennas (reproduced from Kern et al. 2020b) and the expected $T_{\rm rxr}$ for HERA dishes (Fagnoni et al. 2021), respectively.

among other incompleteness scenarios. However, the effect is weaker in $\hat{T}_{\rm rxr}$ compared to temporal gain variations. Finally, in the case of primary beam inaccuracy, the delay spectrum of $\hat{G}$ for the Airy beam is closer to the reference simulation; however, $\hat{T}_{\rm rxr}$ delay spectrum shows additional power on delay modes $\tau < 200$ ns. The effect of beam inaccuracy, on the other hand, is stronger in the case of dipole beam and is similar to the sky-incompleteness effect for $\hat{G}$. The $\hat{T}_{\rm rxr}$ delay spectrum shows excess power on approximately all delay modes below $\tau \sim 600$ ns. This is expected as the dipole beam has a wider field of view than the Airy beam and is more sensitive to off-axis sky temperature. Therefore, uncertainties in the off-axis beam result in relatively large calibration errors and introduces additional spectral structure in calibration products.

## 6 CALIBRATION OF REAL DATA

In this section, we apply the autocorrelation-based calibration method on HERA and EDGES observation data to obtain corresponding $\hat{G}$ and $\hat{T}_{\rm rxr}$.

### 6.1 HERA observations

For this analysis, we use data from the HERA Phase-I (2017–2018) observing cycle during which 47 HERA dishes (with PAPER-type dipole feeds) were operational. We use the observation recorded on Julian Date (JD) 2458 098 and select the 2–10 h LST range and 110–190 MHz frequency band for the analysis. The observation was recorded at time and frequency resolution of 10 s and 97.7 kHz. We further down-select autocorrelations for eight antennas and single polarization (XX) from the observation data. To generate the sky model beam averaged sky temperature model for calibration, we use the GSM2008 sky model and the HERA dipole feed primary beam model from Fagnoni et al. (2021). We also account for the CMB temperature and the ground pickup (assuming a constant ground temperature of 300 K) in the calculation of the sky temperature model to obtain a more realistic calibration model.

Fig. 12 provides a comparison of gain amplitude $|g| = \sqrt{\hat{G}}$ obtained using the method presented here with the gain amplitude obtained by calibrating cross-correlation visibilities as described in Kern et al. (2020a), and a comparison of $\hat{T}_{\rm rxr}$ obtained with expected value of $T_{\rm rxr} \sim 170$ K for the HERA dish with dipole feed (Fagnoni et al. 2021). We observe that the average gain amplitude obtained from autocorrelations matches very well with the frequency smoothed gain amplitude obtained from cross-correlation visibilities of the same data set. On the other hand, $\hat{T}_{\rm rxr}$ is underestimated with a significant bias level compared to the expected value of $T_{\rm rxr}$. We assume the data covariance equal to identity, i.e. $\mathbf{C} = \mathbf{I}$ when determining the calibration parameters. This results in very small fit uncertainties on both $\hat{G}$ and $\hat{T}_{\rm rxr}$ with levels $\sigma_{\rm g} \lesssim 0.1$ and $\sigma_{\rm T} \sim 1$ per cent. We also calibrated the data using the modified calibration (discussed in Section 4.2) to account for any temporal gain that may be present in the data, however it does not impact $|g|$ and slightly improves the $\hat{T}_{\rm rxr}$ estimate but only by a few per cent (plot not shown here). Presence of the spectral structure at ∼30-MHz level in $\hat{T}_{\rm rxr}$ seems to suggest frequency-dependent inaccuracies in the beam model to be the main cause of the bias in $\hat{T}_{\rm rxr}$. Even though this behaviour is similar to the biases observed in the primary beam inaccuracies simulation discussed in Section 4.4, the inaccuracy level used in the simulation does not produce a significantly high bias in $\hat{T}_{\rm rxr}$ compared to the calibration of HERA autocorrelations. Therefore, we suspect that other factors that remain unaccounted for, such as cable reflections, mutual coupling, and ground temperature model, also contribute to the bias in $\hat{T}_{\rm rxr}$ in addition to the primary beam inaccuracies. We expect that incorporating improved beam models (that include mutual coupling and finer frequency sampling) and accounting for other factors in future analyses will mitigate the bias in $\hat{T}_{\rm rxr}$ estimates.

### 6.2 EDGES observations

We also use total power data observed with the EDGES2 instrument for the autocorrelation-based calibration. The data was observed in 2016 (day:260) and used in the analysis in Bowman et al. (2018). Note that we utilize the raw data (uncalibrated) for this analysis. The observation spans the full 24-h LST range and has a time and frequency resolution of 39 s and 6.1 kHz. We down-select the

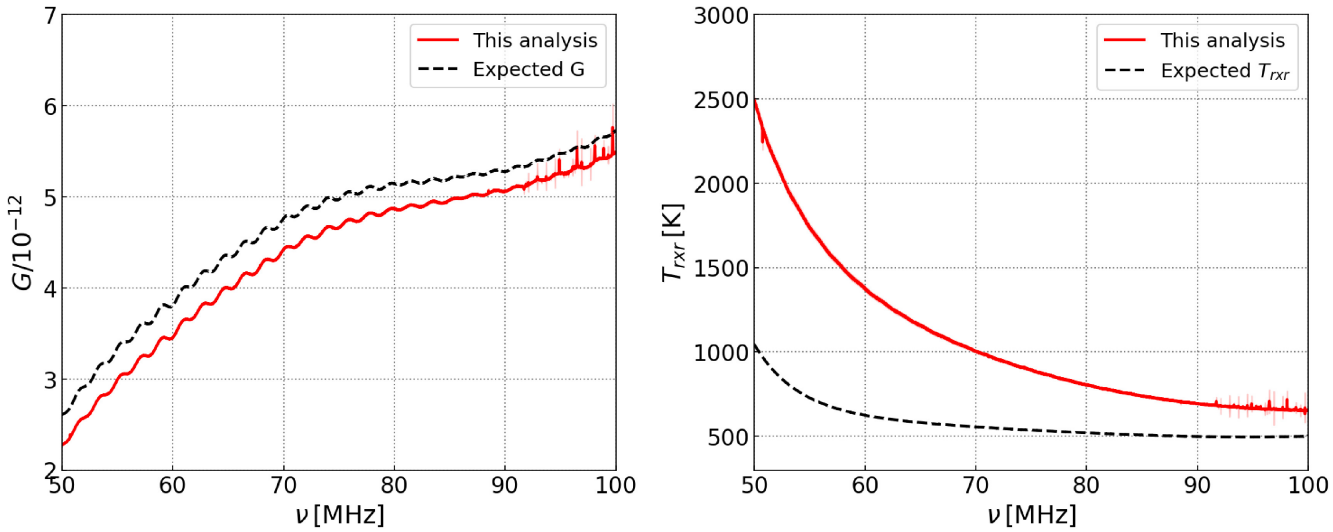


**Figure 13.** $\hat{G}$ (left-hand panel) and $\hat{T}_{\rm rxr}$ (right-hand panel) obtained after calibrating EDGES data. Dashed black curves correspond to expected $G$ and $T_{\rm rxr}$ values obtained by propagating already known three-position switching calibration parameters of EDGES2 receiver system for the observation data used in the analysis.

frequency range of the data to 50–100 MHz. For the calculation of beam averaged sky temperature model ($T_{\rm sky}(\nu, t)$), we use the Haslam 408-MHz sky-map of diffuse emission (Haslam et al. 1982) extrapolated to the frequency range of the EDGES data using a spectral index value $\beta = -2.55$. We also correct for the CMB temperature and the ground pickup to obtain a more accurate model. The primary beam model for average sky temperature calculation is taken from Mahesh et al. (2021) who simulated the EDGES primary beam using the FEKO software package.

The resulting $\hat{G}$ and $\hat{T}_{\rm rxr}$ obtained from calibration are shown in Fig. 13. The expected gain and receiver temperature values are calculated by propagating already known 3-position switching calibration parameters (noise wave parameters and reflection coefficients) for the above observation to obtain equivalent gain and receiver temperature (see e.g. Rogers & Bowman 2012; Monsalve et al. 2017). We find that the gain amplitude $\hat{G}$ is underestimated compared to the expected value. On the other hand, the $\hat{T}_{\rm rxr}$ is highly overestimated compared to the expected value. Bias in $\hat{G}$ and $\hat{T}_{\rm rxr}$ have slow frequency dependence with levels varying between 4–12 and 30–140 per cent, respectively. Similar to the HERA calibration, we assume identity data covariance here, which leads to uncertainties on $\hat{G}$ and $\hat{T}_{\rm rxr}$ between 0.08–0.1 and 0.25–0.5 per cent, respectively, with higher error at the lower frequency end.

We further investigate the cause of the bias in $\hat{G}$ and $\hat{T}_{\rm rxr}$ by changing the sky model used for the calibration of the EDGES data. We repeated the calibration for using the following sky models: extrapolated Haslam map with spectral indices $\beta = -2.5$, $-2.55$, $-2.6$, and $-2.65$ (without CMB temperature correction), and extrapolated GSM2008 map (at 200 MHz) with $\beta = -2.55$. We find that $\hat{T}_{\rm rxr}$ is still overestimated regardless of the choice of the sky model (plots not shown here). However, the overall bias in both $\hat{G}$ and $\hat{T}_{\rm rxr}$ changes with spectral index and the calibration favors the Haslam sky model with a shallower spectral index of $\beta = -2.5$. Changing the spectral index does not affect the noise figure estimate ($\hat{n}$) but results in a different $\hat{G}$ estimate(and hence $\hat{T}_{\rm rxr}$). Furthermore, changing the sky map from Haslam to GSM2008 or GSM2017 for a given spectral index ever so slightly affects the shape of $\hat{G}$ and $\hat{T}_{\rm rxr}$ along frequency but overall bias levels are approximately similar for both cases. In summary, error in fitted noise figure $\hat{n}$ is smooth in frequency and insensitive to changes in the sky spectral index but it is sensitive to changes in spatial structure. In contrast, $\hat{G}$ is affected by both spectral index and the spatial structure of the sky model. The bias in $\hat{G}$ and the frequency smoothness of $\hat{T}_{\rm rxr}$ (similar behaviour observed in simulation discussed in Section 4.3) indicates the sky incompleteness to be the primary cause of the discrepancy between the expected and calibrated values of $G$ and $T_{\rm rxr}$; however, the level of the sky incompleteness used in simulation does not fully explain the bias in $\hat{T}_{\rm rxr}$.

## 7 SUMMARY AND DISCUSSION

Low-frequency 21-cm cosmology experiments aiming to measure the redshifted 21-cm signal from the Cosmic Dawn and Epoch of Reionization require extremely accurate and precise calibration of instruments to extract the faint 21-cm signal from the observed data. However, calibration methods are susceptible to biases and uncertainties due to incompleteness in calibration model e.g. unstable instrumental gains (in time and frequency), incomplete sky model, or primary beam model inaccuracies. Calibration of bandpass amplitude and receiver temperature of instruments using autocorrelations (or total power measurements) against known primary beam and sky-brightness, explored by several 21-cm experiments, is also susceptible to uncertainties and biases due to model incompleteness. We used simulations to investigate various effects that impact the autocorrelation-or total power) based calibration. Our findings are enumerated in the following list and further summarized in Table 1:

(i) Temporal variation in antenna gains introduces a bias in estimated gain and receiver temperature with respect to the time invariant simulation input. The bias in receiver temperature shows a slow spectral dependence. Calibration products for the HERA dish show a weak spectral ripple for all three gain variation scenarios, due to leakage from the HERA primary beam into the passband. The bias is relatively higher for the dipole antenna design, possibly due to larger average uncertainty resulting from its wider field of view.

(ii) We show that it is possible to mitigate the bias in calibration products incurred due to temporal variation. This requires modifying the calibration step to solve for a time-dependent gain and the noise

**Table 1.** A summary of simulation input, calibration output for various model incompleteness effects, error, and bias levels for various incompleteness effects investigated in the analysis.

| Incompleteness effect | Simulation input | Calibration output | Comments |
|---|---|---|---|
| Reference simulation | Constant $G$, fixed $T_{\rm rxr}$, perfect sky model and beam | $\hat{G}$ and $\hat{T}_{\rm rxr}$ without bias and small error | Ideal scenario |
| Temporal gain variation: linear, sine, shifted sine | $G(t)$, fixed $T_{\rm rxr}$, perfect sky model and beam | $\hat{G}$ and $\hat{T}_{\rm rxr}$ with bias | Errors in calibration products larger than the reference simulation |
| Modified calibration with time-dependent gain model | $G(t)$, fixed $T_{\rm rxr}$, perfect sky model and beam | $\langle\hat{G}(t)\rangle_t$ with no observed bias, $\langle\hat{T}_{\rm rxr}(t)\rangle_t$ with no observed bias | rms error (along time) for $\hat{G}(t)$ and $\hat{T}_{\rm rxr}(t)$ is larger than the reference. |
| Sky incompleteness | Constant $G$, fixed $T_{\rm rxr}$, incomplete sky model, perfect beam | $\hat{G}$ and $\hat{T}_{\rm rxr}$ with frequency-dependent bias | Errors in calibration products similar to the reference for HERA beam and slightly larger for dipole beam. |
| Primary beam inaccuracy | Constant $G$, fixed $T_{\rm rxr}$, perfect sky, inaccurate beam | $\hat{G}$ and $\hat{T}_{\rm rxr}$ with frequency-dependent bias | Errors larger than the reference simulation, Airy beam shows small errorr/bias than the dipole beam. |

figure rather than solving for a single gain and noise figure value per frequency channel. We show that using a first-order polynomial model for gain and noise figure in calibration mitigates the bias incurred due to linear variation of antenna gain. However, the modified calibration increases the rms noise levels in recovered gain and receiver temperature by a factor of a few.

(iii) Using an incomplete sky model for calibration introduces spectral structure in the estimated gain and receiver temperature that depends on the level of incompleteness. Both antenna designs are similarly impacted by this effect.

(iv) Inaccuracies in primary beam model used in calibration also lead to frequency-dependent bias in the estimated gain and receiver temperature. However, the bias is significantly smaller for the Airy beam than the dipole beam that has a wider field of view. This is mainly due to lower off-axis sensitivity of the Airy beam compared to a dipole beam. This, combined with off-axis errors in the dipole primary beam results in larger bias.

(v) The delay spectrum analysis confirms the leakage of power to non-zero delay modes suggesting that various model-incompleteness effects introduce spectral structure to calibration products.

(vi) We also show the application of autocorrelation-based calibration on real HERA and EDGES data. The gain amplitudes obtained for HERA autocorrelations match well with the gain amplitudes obtained from calibration of HERA cross-correlation visibilities. However, the receiver temperatures are severely underestimated compared to expected values. Although we suspect this to be caused by primary beam inaccuracies as shown by the simulation, the inaccuracy level used in simulation does not explain bias level in the HERA receiver temperature. Possible contribution from other unaccounted factors such as mutual coupling, cable reflections, ground temperature model may explain the unexpected bias level in HERA receiver temperature.

(vii) Calibration products for EDGES data disagree with the EDGES internal calibration but in the opposite sense from HERA. In the case of EDGES, the noise figure and hence the receiver temperature is overestimated. The fitted noise figure varies most strongly when changing between different spatial models (e.g. Haslam versus GSM2008) and not at all when changing the spectral index for a given sky model. This suggest the spatial accuracy of the sky catalog to be more relevant than the spectral index. We left the exploration of beam model variations and their effect on EDGES and HERA data calibration for analyses.

In summary, we find that autocorrelation-based calibration is sensitive to model inaccuracies like temporal gain variations, sky incompleteness and primary beam inaccuracies. Applying the calibration method to data from HERA and EDGES we find small biases in gain and larger unexpected offsets in receiver temperature. The behaviour of these offsets are similar to those found when injecting model error into simulation; however, the latter does not completely explain the scale of the offsets in receiver temperatures obtained from calibration of both instruments. We show that it is possible to mitigate bias caused by temporal gain variations by using higher order temporal polynomials to represent the calibration products. Mitigation of errors due to sky and beam inaccuracies will improve with refined models of those factors.

## ACKNOWLEDGEMENTS

This work was supported by the National Science Foundation through awards for HERA (AST-1836019) and EDGES (AST-1813850, AST-1609450, and AST-1908933). NM was supported by the Future Investigators in NASA Earth and Space Science and Technology (FINESST) cooperative agreement 80NSSC19K1413. DL was supported by the NASA Solar System Exploration Virtual Institute Cooperative Agreement number 80ARC017M0006. N. Kern gratefully acknowledges support from the MIT Pappalardo Fellowship. HERA is hosted by the South African Radio Astronomy Observatory, which is a facility of the National Research Foundation, an agency of the Department of Science and Innovation. EDGES is located at the Murchison Radio-astronomy Observatory. We acknowledge the Wajarri Yamatji people as the traditional owners of the Observatory site. We thank CSIRO for providing site infrastructure and support. This analysis makes use of following software packages (publicly-available and open-source): PYGDSM(https://github.com/telegraphic/pygdsm), HEALPY (https://pypi.org/project/healpy/), EPHEM (https://pypi.org/project/ephem/), NUMPY (https://numpy.org/), SCIPY (https://www.scipy.org/), and MATPLOTLIB (https://matplotlib.org/).

## DATA AVAILABILITY

The data underlying this paper will be shared on reasonable request to the corresponding author.

## REFERENCES

An H., Nauwelaers B., Van de Capelle A., 1993, Electron. Lett., 29, 1594
Asad K. M. B. et al., 2021, MNRAS, 502, 2970
Baars J. W. M., Genzel R., Pauliny-Toth I. I. K., Witzel A., 1977, A&A, 500, 135

Barry N. et al., 2019, ApJ, 884, 1
Barry N., Hazelton B., Sullivan I., Morales M. F., Pober J. C., 2016, MNRAS, 461, 3135
Berger P. et al., 2016, in Helen J. H., Roberto G., Heather K. M., eds, Proc. SPIE Conf. Ser., Vol. 9906, Ground-based and Airborne Telescopes VI, SPIE, Bellingham, p. 16
Bernardi G. et al., 2016, MNRAS, 461, 2847
Bowman J. D. et al., 2007, AJ, 133, 1505
Bowman J. D. et al., 2013, Publ. Astron. Soc. Aust., 30, e031
Bowman J. D., Rogers A. E. E., Monsalve R. A., Mozdzen T. J., Mahesh N., 2018, Nature, 555, 67
Chang C., Monstein C., Refregier A., Amara A., Glauser A., Casura S., 2015, PASP, 127, 1131
Cohen A. S., Lane W. M., Cotton W. D., Kassim N. E., Lazio T. J. W., Perley R. A., Condon J. J., Erickson W. C., 2007, AJ, 134, 1245
DeBoer D. R. et al., 2017, PASP, 129, 045001
De Oliveira-Costa A., Tegmark M., Gaensler B. M., Jonas J., Landecker T. L., Reich P., 2008, MNRAS, 388, 247(GSM2008)
Dowell J., Taylor G. B., Schinzel F. K., Kassim N. E., Stovall K., 2017, MNRAS, 469, 4537
Eastwood M. W. et al., 2018, AJ, 156, 32
Eastwood M. W. et al., 2019, AJ, 158, 84
Ewall-Wice A. et al., 2016, MNRAS, 460, 4320
Ewall-Wice A., Dillon J. S., Liu A., Hewitt J., 2017, MNRAS, 470, 1849
Fagnoni N. et al., 2021, MNRAS, 500, 1232
Haslam C. G. T., Salter C. J., Stoffel H., Wilson W. E., 1982, A&AS, 47, 1
Heald G. H. et al., 2015, A&A, 582, A123
Hurley-Walker N. et al., 2016, MNRAS, 464, 1146
Iheanetu K., Girard J. N., Smirnov O., Asad K. M. B., de Villiers M., Thorat K., Makhathini S., Perley R. A., 2019, MNRAS, 485, 4107
Jacobs D. C. et al., 2017, PASP, 129, 035002
Kern N. S. et al., 2020a, ApJ, 888, 70
Kern N. S. et al., 2020b, ApJ, 890, 122
Kern N. S., Parsons A. R., Dillon J. S., Lanman A. E., Fagnoni N., de Lera Acedo E., 2019, ApJ, 884, 105
Kolopanis M. et al., 2019, ApJ, 883, 133
Koopmans L. et al., 2015, Advancing Astrophysics with the Square Kilometre Array (AASKA14). Proc. Sci., Trieste, p. PoS#001
Li W. et al., 2018, ApJ, 863, 170
Li W. et al., 2019, ApJ, 887, 141
Li Y., Santos M. G., Grainge K., Harper S., Wang J., 2021, MNRAS, 501, 4344
Line J. L. B. et al., 2018, Publ. Astron. Soc. Aust., 35, 45
Liu A., Parsons A. R., Trott C. M., 2014, Phys. Rev. D, 90, 023018
Mahesh N., Bowman J. D., Mozdzen T. J., Rogers A. E. E., Monsalve R. A., Murray S. G., Lewis D., 2021, AJ, 162, 38
Mellema G. et al., 2013, Exp. Astron., 36, 235
Mertens F. G. et al., 2020, MNRAS, 493, 1662
Mitchell D. A., Greenhill L. J., Wayth R. B., Sault R. J., Lonsdale C. J., Cappallo R. J., Morales M. F., Ord S. M., 2008, IEEE J. Sel. Top. Signal Proces., 2, 707
Monsalve R. A. et al., 2021, ApJ, 908, 145
Monsalve R. A., Rogers A. E. E., Bowman J. D., Mozdzen T. J., 2017, ApJ, 835, 49
Mozdzen T. J., Mahesh N., Monsalve R. A., Rogers A. E. E., Bowman J. D., 2019, MNRAS, 483, 4411
Neben A. R. et al., 2015, Radio Sci., 50, 614
Neben A. R. et al., 2016, ApJ, 826, 199
Nunhokee C. D. et al., 2020, ApJ, 897, 5
Paciga G. et al., 2011, MNRAS, 413, 1174
Parsons A. R. et al., 2010, AJ, 139, 1468
Parsons A. R., Pober J. C., Aguirre J. E., Carilli C. L., Jacobs D. C., Moore D. F., 2012, ApJ, 756, 165
Patil A. H. et al., 2016, MNRAS, 463, 4317
Patra N. et al., 2018, Exp. Astron., 45, 177
Pauliny-Toth I. K., Shakeshaft J. R., 1962, MNRAS, 124, 61
Philip L. et al., 2019, J. Astron. Instrum., 8, 1950004
Rogers A. E. E., Bowman J. D., 2012, Radio Sci., 47, RS0K06
Rogers A. E. E., Pratap P., Kratzenberg E., Diaz M. A., 2004, Radio Sci., 39, RS2023
Salvini S., Wijnholds S. J., 2014, A&A, 571, A97
Shimwell T. W. et al., 2017, A&A, 598, A104
Shimwell T. W. et al., 2019, A&A, 622, A1
Singh S. et al., 2017, ApJ, 845, L12
Singh S., Subrahmanyan R., Shankar N. U., Rao M. S., Girish B. S., Raghunathan A., Somashekar R., Srivani K. S., 2018, Exp. Astron., 45, 269
Thyagarajan N., Parsons A. R., DeBoer D. R., Bowman J. D., Ewall-Wice A. M., Neben A. R., Patra N., 2016, ApJ, 825, 9
Tingay S. J. et al., 2013, Publ. Astron. Soc. Aust., 30, e007
Trott C. M. et al., 2016, ApJ, 818, 139
van Haarlem M. P. et al., 2013, A&A, 556, A2
Wang J. et al., 2021, MNRAS, 505, 3698
Wilson T. L., Rohlfs K., Hüttemeister S., 2009, Tools of Radio Astronomy. Springer, Berlin
Yatawatta S., 2015, MNRAS, 449, 4506
Zarka P., Girard J. N., Tagger M., Denis L., 2012, in Boissier S., de Laverny P., Nardetto N., Samadi R., Valls-Gabaud D., Wozniak H., eds, SF2A-2012: Proceedings of the Annual meeting of the French Society of Astronomy and Astrophysics. Socié té Francaise d'Astronomie et d'Astrophysique, Nice, p. 687
Zheng H. et al., 2017, MNRAS, 464, 3486(GSM2016)

[1]*School of Earth and Space Exploration, Arizona State University, Tempe, AZ 85287, USA*
[2]*Department of Physics, Winona State University, Winona, MN 55987, USA*
[3]*Department of Astronomy, University of California, Berkeley, CA 94720, USA*
[4]*Department of Physics and Astronomy, University of Pennsylvania, Philadelphia, PA 19104, USA*
[5]*Cavendish Astrophysics, University of Cambridge, Cambridge CB2 8PQ, UK*
[6]*South African Radio Astronomy Observatory, Black River Park, 2 Fir Street, Observatory, Cape Town 7925, South Africa*
[7]*Department of Physics and Electronics, Rhodes University, PO Box 94, Grahamstown 6140, South Africa*
[8]*INAF – Istituto di Radioastronomia, via Gobetti 101, I-40129 Bologna, Italy*
[9]*National Radio Astronomy Observatory, Charlottesville, VA 22903, USA*
[10]*Queen Mary University London, London E1 4NS, UK*
[11]*Department of Physics, Brown University, Providence, RI 02912, USA*
[12]*National Radio Astronomy Observatory, Socorro, NM 87801, USA*
[13]*Department of Physics and MIT Kavli Institute for Astrophysics and Space Research, MIT, Cambridge, MA 02139, USA*
[14]*Department of Physics and Astronomy, University of California, Los Angeles, CA 90095, USA*
[15]*School of Physics, University of Melbourne, Parkville, VIC 3010, Australia*
[16]*Department of Physics, University of Washington, Seattle, WA 98195, USA*
[17]*eScience Institute, University of Washington, Seattle, WA 98195, USA*
[18]*School of Chemistry and Physics, University of KwaZulu-Natal, Westville Campus, Private Bag X54001, Durban, USA*
[19]*Department of Physics and McGill Space Institute, McGill University, 3600 University Street, Montreal, QC H3A 2T8, Canada*
[20]*School of Chemistry and Physics, University of KwaZulu-Natal, Westville Campus, Durban 4000, South Africa*
[21]*Scuola Normale Superiore, I-56126 Pisa, PI, Italy*
[22]*Facultad de Ingeniería, Universidad Católica de la Santísima Concepción, Alonso de Ribera 2850, Concepción, Chile*
[23]*Department of Physics and Astronomy, University of Western Cape, Cape Town 7535, South Africa*
[24]*Center for Astrophysics, Harvard & Smithsonian, Cambridge, MA 02138, USA*
[25]*American Astronomical Society,Washington, DC 20006, USA*

This paper has been typeset from a TEX/LATEX file prepared by the author.